J. Fluid Mech. (2002), *vol.* 452, *pp.* 61–96.
DOI: 10.1017/S0022112001006619 Printed in the United Kingdom

Analysis of drag and virtual mass forces in bubbly suspensions using an implicit formulation of the lattice Boltzmann method

By K. SANKARANARAYANAN, X. SHAN†, I. G. KEVREKIDIS AND S. SUNDARESAN

Department of Chemical Engineering,
Princeton University, Princeton, NJ 08544, USA

(Received 26 July 2000 and in revised form 30 July 2001)

We present closures for the drag and virtual mass force terms appearing in a two-fluid model for flow of a mixture consisting of uniformly sized gas bubbles dispersed in a liquid. These closures were deduced through computational experiments performed using an implicit formulation of the lattice Boltzmann method with a BGK collision model. Unlike the explicit schemes described in the literature, this implicit implementation requires iterative calculations, which, however, are local in nature. While the computational cost per time step is modestly increased, the implicit scheme dramatically expands the parameter space in multiphase flow calculations which can be simulated economically. The closure relations obtained in our study are limited to a regular array of uniformly sized bubbles and were obtained by simulating the rise behaviour of a single bubble in a periodic box. The effect of volume fraction on the rise characteristics was probed by changing the size of the box relative to that of the bubble. While spherical bubbles exhibited the expected hindered rise behaviour, highly distorted bubbles tended to rise cooperatively. The closure for the drag force, obtained in our study through computational experiments, captured both hindered and cooperative rise. A simple model for the virtual mass coefficient, applicable to both spherical and distorted bubbles, was also obtained by fitting simulation results. The virtual mass coefficient for isolated bubbles could be correlated with the aspect ratio of the bubbles.

1. Introduction

Two-phase flows consisting of gas bubbles dispersed in a liquid are commonly encountered in industrial devices such as chemical reactors and separators (Fan & Tsuchiya 1990; van Baten & Krishna 2000). Various regimes of flow, ranging from gently rising bubble swarms to churn-turbulent flow, are commonly observed in these devices. It is generally accepted that the performance and scale-up characteristics of these devices are strongly influenced by macro-scale coherent structures (van den Akker 1998), and consequently there is much interest in simulating flow structures occurring on a length scale much larger than the individual bubbles.

A hydrodynamic model that treats the gas and liquid phases in a bubbly suspension

† Present address: Microsoft Corporation, Redmond, WA 98052, USA.

as inter-penetrating continua may be written as

$$\frac{\partial \rho_g \phi}{\partial t} + \nabla \cdot (\rho_g \phi \boldsymbol{u}_g) = 0, \tag{1}$$

$$\frac{\partial \rho_l (1-\phi)}{\partial t} + \nabla \cdot (\rho_l (1-\phi) \boldsymbol{u}_l) = 0, \tag{2}$$

$$\rho_g \phi \left[\frac{\partial \boldsymbol{u}_g}{\partial t} + \boldsymbol{u}_g \cdot \nabla \boldsymbol{u}_g \right] = \phi \nabla \cdot \boldsymbol{\Pi}_l + \nabla \cdot \boldsymbol{\Pi}_g + \boldsymbol{F} + \phi \rho_g \boldsymbol{g}, \tag{3}$$

$$\rho_l (1-\phi) \left[\frac{\partial \boldsymbol{u}_l}{\partial t} + \boldsymbol{u}_l \cdot \nabla \boldsymbol{u}_l \right] = (1-\phi) \nabla \cdot \boldsymbol{\Pi}_l - \boldsymbol{F} + (1-\phi) \rho_l \boldsymbol{g}, \tag{4}$$

where ρ_l and ρ_g are the densities of the liquid and gas phases, respectively; $\boldsymbol{u}_g$ and $\boldsymbol{u}_l$ are the local average velocities; $\boldsymbol{\Pi}_g$ and $\boldsymbol{\Pi}_l$ are the effective stress tensors; $\boldsymbol{F}$ is the interaction force per unit volume of the mixture; $\boldsymbol{g}$ is the specific gravity force and ϕ is the volume fraction of bubbles. Closure relations for $\boldsymbol{\Pi}_g$, $\boldsymbol{\Pi}_l$ and $\boldsymbol{F}$ must be postulated before the hydrodynamic model can be used to simulate suspension flows. Drag, virtual mass and lift forces are usually the major components of the inter-phase interaction force (see, for example, Jakobsen *et al.* 1997).

The local volume- and mass-average velocities of the mixture ($\boldsymbol{u}_v$ and $\boldsymbol{u}_m$, respectively) are given by

$$\boldsymbol{u}_v = \phi \boldsymbol{u}_g + (1-\phi) \boldsymbol{u}_l, \quad \boldsymbol{u}_m = (\rho_g \phi \boldsymbol{u}_g + \rho_l (1-\phi) \boldsymbol{u}_l) / \bar{\rho}, \tag{5}$$

where $\bar{\rho} = \rho_g \phi + \rho_l (1-\phi)$. Alternative forms of the hydrodynamic model, expressed in terms of any two independent velocities (e.g. $\boldsymbol{u}_m$ and $\boldsymbol{u}_l$ (Spelt & Sangani 1998) instead of $\boldsymbol{u}_g$ and $\boldsymbol{u}_l$), can be constructed by linear combination of (1)–(4). In every form of the continuum model, the issue of closure for the effective stresses and interphase interaction force remains. A great deal of work on deriving closures for these terms has been described in the literature (e.g. see Drew 1971; Drew & Segel 1971; Nigmatulin 1979; Sangani, Zhang & Prosperetti 1991; Sangani & Didwania 1993*a*,*b*; Zhang & Prosperetti 1994; Bulthuis, Prosperetti & Sangani 1995; Zhang & Prosperetti 1997; Kang *et al.* 1997; Spelt & Sangani 1998). All these closures are limited to swarms of uniformly sized bubbles. Furthermore, the analyses of effective stresses are restricted to either low Reynolds number (see e.g. Zhang & Prosperetti 1994) or potential flow limits (e.g. Spelt & Sangani 1998), while the available closures for virtual mass force are based only on potential flow theory (Lamb 1932; van Wijngaarden 1976; Auton, Hunt & Prud'homme 1988; Biesheuvel & Spoelstra 1989; Felderhof 1991; Spelt & Sangani 1998). The influence of wakes behind the bubbles on the motion of the swarm is hardly mentioned in the closure relations described in the literature.

In the present manuscript, we describe the results of computational experiments on rise of a single bubble in periodic boxes of various sizes under the action of buoyancy, which have been used to deduce closures for drag and virtual mass forces for such an ordered array of bubbles. Our flow simulations are based on the lattice Boltzmann method (LBM), which is a useful alternative to numerically approximating the solutions of continuum equations describing fluid flow (Chen & Doolen 1998). This technique has been applied to problems ranging from single species–single component flow to multicomponent multiphase flow (see e.g. Gustensen *et al.* 1991; Shan & Chen 1993; Shan & Doolen 1995; Swift, Osborn & Yeomans 1995; Swift *et al.* 1996; Kato *et al.* 1997; Chen & Doolen 1998; Shan & He 1998; He, Shan & Doolen 1998; Sankara-

narayanan *et al.* 1999). A desirable feature of LBM is that the computations are local, which makes implementation of the scheme on parallel platforms easy. The LBM evolution schemes described in the literature typically involve explicit marching in time.

LBM is an attractive technique for simulating multiphase flows involving free surfaces, such as the problem of bubble motion that we are concerned with in this paper. In our efforts to study such problems, we found that a slightly modified LBM scheme requiring only local iterative calculations dramatically expanded the physical parameter space that can be explored efficiently. The important dimensionless groups encountered in the problem of bubble rise under the action of gravity are the Reynolds number ($Re = vd_e/\nu$), the Morton number ($Mo = g\rho^2\Delta\rho\nu^4/\sigma^3$) and the Eötvös number ($Eo = g\Delta\rho d_e^2/\sigma$). In these ρ denotes the density of the continuous (liquid) phase, d_e is the effective diameter of the gas bubble, v is the rise velocity of the bubble, g is the acceleration due to gravity, ν is the liquid kinematic viscosity, σ is the interfacial tension and $\Delta\rho$ denotes the density difference between the continuous (liquid) and dispersed (gas) phases. When Eo is small, the rising bubbles are nearly spherical, while at larger Eo values the bubbles are highly distorted. The Morton number is a physical property group characterizing the gas–liquid system and does not involve any dynamic or bubble-size-dependent quantities. The Weber number can easily be constructed as a combination of the other groups: $We = Re^2(Mo/Eo)^{1/2}$.

Gas–liquid systems encountered in nature and in industrial practice range from $Mo = 10^{-12}$ (tap water–air) to $Mo = 10^5$ (corn syrup–air). Re ranges from $\ll 1$ to 10^3, while $10^{-2} < Eo < 10^4$ (Fan & Tsuchiya 1990). In LBM simulations, choosing conditions such that Mo is very small and Eo is large is a challenge. The condensed-phase density ρ, density difference $\Delta\rho$ and interfacial tension, σ, all in lattice units, can be varied only to a limited extent (more on this later). Thus, small Mo values can be obtained only by choosing small g or ν; varying g corresponds to changing buoyancy, the driving force for the flow. Too small a value of g implies that large Eo can be obtained only if the bubble spans many lattice nodes (i.e. large d_e); this renders the calculation computationally very expensive. A more effective means of achieving small Mo values is to set ν to be small, as Eo is independent of ν. In LBM implementations using the BGK collision model, ν is proportional to the relaxation time, τ. Decreasing τ too much renders the explicit LBM scheme numerically unstable (see Worthing, Mozer & Seeley 1997; Sterling & Chen 1996; Lallemand & Luo 2000), and this numerical instability problem is more severe in multiphase flow simulations than in single-phase flow calculations. The implicit LBM scheme described in this paper did not manifest this numerical instability, and we were able to simulate bubble dynamics over a very broad range of Mo and Eo values.

Sections 2 and 3 of this paper describe explicit and implicit LBM-BGK schemes, respectively. A simple analysis, in § 4, of density variation in the vicinity of a planar gas–liquid interface is used to illustrate that a key assumption in the derivation of the LBM equations based on the Martys, Shan & Chen (1998), Shan & Chen (1993), He *et al.* (1998) approach is satisfied more accurately by the implicit scheme.

Using the implicit scheme, we have simulated the rise of bubbles in spatially periodic domains, spanning a wide range of Mo and Eo. These results, presented in § 5, are then used to extract closure relations for interphase drag. Computational experiments to probe the closure for the virtual mass force are described in § 6. The effects of the orientation of gravity relative to the periodic arrangement of bubbles on the interphase drag and virtual mass are discussed in § 7. A limited exploration of the rise behaviour of multiple bubbles in a periodic box is presented in § 8. The key points of the paper are summarized in § 9.

2. The lattice Boltzmann method

We adopt the view that the LBM is based on a finite difference discretization of the continuum Boltzmann-BGK equation (see e.g. Bhatnagar, Gross & Krook 1954; He & Luo 1997*a*,*b*) which describes the evolution of the single-particle distribution function, $f(\boldsymbol{x}, \boldsymbol{\xi}, t)$ in the position ($\boldsymbol{x}$)–velocity ($\boldsymbol{\xi}$) phase space. Consider the single-species Boltzmann-BGK equation

$$\frac{\partial f}{\partial t} + \boldsymbol{\xi} \cdot \nabla_x f + \boldsymbol{a} \cdot \nabla_\xi f = -\frac{f - f^{(0)}}{\lambda}, \tag{6}$$

where λ is the relaxation time due to collisions, $\boldsymbol{a}$ is the force per unit mass acting on the particles, and $f^{(0)} = f^{(0)}(\rho, \boldsymbol{u}, T)$ is the Maxwell–Boltzmann equilibrium distribution function:

$$f^{(0)} = n \left(\frac{m}{2\pi k_B T} \right)^{D/2} \exp \left[-\frac{m|\boldsymbol{\xi} - \boldsymbol{u}|^2}{2k_B T} \right] \tag{7}$$

in which k_B is the Boltzmann constant, D is the dimension of the space, m is the mass of the particle and n, $\boldsymbol{u}$, and T are the macroscopic number density, velocity and temperature, respectively. These quantities, and the mass density ρ, are calculated from successive moments of the distribution function:

$$n = \int f \, \mathrm{d}\boldsymbol{\xi}, \quad \rho = mn, \quad \rho \boldsymbol{u} = m \int \boldsymbol{\xi} f \, \mathrm{d}\boldsymbol{\xi}, \quad \frac{D}{m} \rho k_B T = m \int |\boldsymbol{\xi} - \boldsymbol{u}|^2 f \, \mathrm{d}\boldsymbol{\xi}. \tag{8}$$

We non-dimensionalize (6) and (7) using a reference temperature T_0, mass m_0, velocity $c_s = \sqrt{k_B T_0 / m_0}$, which is the speed of sound in an ideal gas consisting of molecules with mass m_0 at temperature T_0, and a (as yet unspecified) reference time t_s:

$$\frac{\partial \hat{f}}{\partial \hat{t}} + \hat{\boldsymbol{\xi}} \cdot \hat{\nabla}_x \hat{f} + \hat{\boldsymbol{a}} \cdot \hat{\nabla}_\xi \hat{f} = -\frac{\hat{f} - \hat{f}^{(0)}}{\tilde{\tau}} \tag{9}$$

where $\tilde{\tau} = \lambda / t_s$, $\hat{f}^{(0)}$ is given by

$$\hat{f}^{(0)} = \hat{n} \left(\frac{1}{2\pi\theta} \right)^{D/2} \exp \left[-\frac{|\hat{\boldsymbol{\xi}} - \hat{\boldsymbol{u}}|^2}{2\theta} \right] \tag{10}$$

and the carets denote non-dimensional quantities. Here θ is the scaled temperature, defined as $\theta = m_0 T / m T_0$. We now drop the carets for convenience. Equation (8) takes the following form:

$$n = \int f \, \mathrm{d}\boldsymbol{\xi}, \quad \rho = mn, \quad n\boldsymbol{u} = \int \boldsymbol{\xi} f \, \mathrm{d}\boldsymbol{\xi}, \quad Dn\theta = \int |\boldsymbol{\xi} - \boldsymbol{u}|^2 f \, \mathrm{d}\boldsymbol{\xi}. \tag{11}$$

Following Shan & Doolen (1993), Martys *et al.* (1998) and He *et al.* (1998) we first approximate $\boldsymbol{a} \cdot \nabla_\xi f$ by $\boldsymbol{a} \cdot \nabla_\xi f^{(0)}$ and absorb it into the Maxwellian to obtain

$$\frac{\partial f}{\partial t} + \boldsymbol{\xi} \cdot \nabla_x f = -\frac{f - f^{(eq)}}{\tilde{\tau}}, \tag{12}$$

where $f^{(eq)} = f^{(0)}(n, \boldsymbol{u} + \boldsymbol{a}\tilde{\tau}, \theta)$. Equation (12) can be integrated over a time step δt (He & Luo 1997*a*,*b*):

$$f(\boldsymbol{x} + \boldsymbol{\xi}\delta t, \boldsymbol{\xi}, t + \delta t) - f(\boldsymbol{x}, \boldsymbol{\xi}, t) = -\int_t^{t+\delta t} \frac{f - f^{(eq)}}{\tilde{\tau}} \, \mathrm{d}t. \tag{13}$$

Different integration techniques can be used to handle the right-hand side. In the explicit LBM, the integrand is evaluated at time t leading to

$$f(\boldsymbol{x}+\boldsymbol{\xi}\delta t,\boldsymbol{\xi},t+\delta t)-f(\boldsymbol{x},\boldsymbol{\xi},t)=-\frac{f(\boldsymbol{x},\boldsymbol{\xi},t)-f^{eq}(\boldsymbol{x},\boldsymbol{\xi},t)}{\tau} \tag{14}$$

with $\tau=\tilde{\tau}/\delta t$, and the understanding that $f^{(eq)}(\boldsymbol{x},\boldsymbol{\xi},t)$ is evaluated using $n(\boldsymbol{x},t)$, $\boldsymbol{u}(\boldsymbol{x},t)$ and $\theta(\boldsymbol{x},t)$.

Using Hermite discretization of the velocity space (Shan & He 1998), (14) can be written as

$$f_i(\boldsymbol{x}+\boldsymbol{e}_i,t+1)-f_i(\boldsymbol{x},t)=-\frac{f_i(\boldsymbol{x},t)-f_i^{(eq)}(\boldsymbol{x},t)}{\tau}, \tag{15}$$

where δt has been set to unity. Here, f_i are related to $f(\boldsymbol{x},\boldsymbol{\xi},t)$ through $f_i=w_i/\omega(\boldsymbol{\xi}_i)f(\boldsymbol{x},\boldsymbol{\xi}_i,t)$, where w_i is a weight, $\omega(\boldsymbol{\xi})=(1/2\pi)^{D/2}\exp[-\frac{1}{2}\boldsymbol{\xi}\cdot\boldsymbol{\xi}]$ is the chosen weight function and $\boldsymbol{e}_i=\boldsymbol{\xi}_i$ are the abscissas of the quadrature in velocity space given by (Stroud 1971)

$$\boldsymbol{\xi}_i=\begin{cases}(0,0), & i=0,\\ (\cos\phi_i,\sin\phi_i)\sqrt{3}, & \phi_i=(i-1)\pi/2, \quad i=1\text{–}4,\\ (\cos\phi_i,\sin\phi_i)\sqrt{6}, & \phi_i=(i-5)\pi/2+\pi/4, \quad i=5\text{–}8\end{cases} \tag{16}$$

in two dimensions and

$$\boldsymbol{\xi}_i=\begin{cases}(0,0,0), & i=0,\\ (\pm\sqrt{3},0,0),(0,\pm\sqrt{3},0),(0,0,\pm\sqrt{3}), & i=1\text{–}6,\\ (\pm\sqrt{3},\pm\sqrt{3},\pm\sqrt{3}), & i=7\text{–}14\end{cases} \tag{17}$$

in three dimensions. The physical space thus assumes the form of a square lattice in two dimensions and a cubic one in three dimensions, with lattice spacing $\sqrt{3}$. Through a Chapman–Enskog analysis of (15), it can be shown (Huang 1987) that the Navier–Stokes equations can be recovered at the low Mach number limit with a scaled kinematic viscosity, $\nu=\tau-\frac{1}{2}$. It has been shown (Shan & He 1998) that a second-order Hermite polynomial approximation for the equilibrium distribution, $f^{(eq)}$, is sufficient for isothermal flow calculations:

$$f_i^{(eq)}=w_i n[1+\gamma_i+\boldsymbol{e}_i\cdot(\boldsymbol{u}+\tau\boldsymbol{a})+\tfrac{1}{2}(\boldsymbol{e}_i\cdot(\boldsymbol{u}+\tau\boldsymbol{a}))^2-\tfrac{1}{2}(\boldsymbol{u}+\tau\boldsymbol{a})\cdot(\boldsymbol{u}+\tau\boldsymbol{a})], \tag{18}$$

where $\gamma_i=(\boldsymbol{e}_i\cdot\boldsymbol{e}_i-D)(\theta-1)/2$, while a higher-order approximation is needed if the energy equation is to be recovered. In two dimensions the weights w_i are

$$w_i=\begin{cases}4/9, & i=0,\\ 1/9, & i=1\text{–}4,\\ 1/36, & i=5\text{–}8\end{cases} \tag{19}$$

and in three dimensions they are

$$w_i=\begin{cases}2/9, & i=0,\\ 1/9, & i=1\text{–}6,\\ 1/72, & i=7\text{–}14,\end{cases} \tag{20}$$

In terms of f_i, the moments in (11) take the form

$$n=\sum_{i=0}^{P}f_i, \quad n\boldsymbol{u}=\sum_{i=0}^{P}f_i\boldsymbol{e}_i, \quad n\theta D=\sum_{i=0}^{P}f_i(\boldsymbol{e}_i-\boldsymbol{u})\cdot(\boldsymbol{e}_i-\boldsymbol{u}). \tag{21}$$

In the explicit LBM, i.e. equations (15)–(21), all operations are local and no

iterations are necessary. However, this scheme becomes numerically unstable as $\nu \to 0$, or equivalently, $\tau \to \frac{1}{2}$. A detailed discussion of the stability of this scheme can be found in Worthing *et al.* (1997), Sterling & Chen (1996) and Lallemand & Luo (2000). In some applications, such as simulation of flow of bubbly suspensions described below, this instability severely limits our ability to access practically relevant regions of parameter space. This prompted us to seek an alternative approximation for equation (13).

3. Implicit LBM-BGK evolution equation

Consider an implicit LBM-BGK evolution equation obtained by evaluating the right-hand side of (13) by a trapezoidal rule and setting δt to unity:

$$f_i(\boldsymbol{x}+\boldsymbol{e}_i, t+1) - f_i(\boldsymbol{x}, t) = -\frac{\frac{1}{2}f_i(\boldsymbol{x}, t) + \frac{1}{2}f_i(\boldsymbol{x}+\boldsymbol{e}_i, t+1) - \frac{1}{2}f_i^{(eq)}(\boldsymbol{x}, t) - \frac{1}{2}f_i^{(eq)}(\boldsymbol{x}+\boldsymbol{e}_i, t+1)}{\tau}. \tag{22}$$

This, coupled with equations (16)–(21), henceforth referred to as the implicit LBM, clearly requires iterative calculations. These iterations are, however, local in nature: iterations at each node can be done independent of other nodes. Thus, the incremental cost of the calculations is minimal. This extra effort, however, expands in a dramatic manner the range of parameter space in simulation of gas–liquid flow which can be investigated efficiently. It can be shown readily that (22) reduces to the Navier–Stokes equations in the low Mach number limit, with a scaled kinematic viscosity $\nu = \tau$.

In the examples that we present below, gas bubbles and the surrounding liquid medium are generated as coexisting phases of a multi-component mixture with a non-ideal equation of state. Large gas bubbles, as they rise through the liquid, will become highly distorted; this non-uniformity in the curvature of the interfacial region can give rise to appreciable condensation and evaporation in regions of high and low curvature, respectively. Condensation and evaporation, however, are typically not appreciable in systems of engineering interest we address, such as air bubbles rising in (non-boiling) water . We chose to model these through a two-component (and again two-phase) system, in which the species interaction parameters have been tailored to keep one component preferentially in the gas phase and the other component in the liquid.

The generalization of explicit LBM-BGK to multicomponent systems, and the manner in which a non-ideal equation of state is handled are described in the literature (Shan & Chen 1993; Shan & Doolen 1995; Shan & He 1998; He *et al.* 1998). These apply for the implicit LBM-BGK as well, and we only present here a brief outline essential for describing our results.

We consider a two-component system with single relaxation time ($\tau_1 = \tau_2 = \tau$), a single mass ($m_1 = m_2 = m$) and limit ourselves to isothermal examples ($\theta = 1$). Equation (15) of the explicit scheme applies for each species α:

$$f_i^{\alpha}(\boldsymbol{x}+\boldsymbol{e}_i, t+1) - f_i^{\alpha}(\boldsymbol{x}, t) = -\frac{f_i^{\alpha}(\boldsymbol{x}, t) - f_i^{\alpha(eq)}(\boldsymbol{x}, t)}{\tau^{\alpha}} \tag{23}$$

and equation (22) in the implicit scheme is written for each species similarly. Equations (21) and (18) now take the form

$$n^{\alpha} = \sum_{i=0}^{P} f_i^{\alpha}, \quad n = \sum_{\alpha=1}^{2} n^{\alpha}, \quad n\boldsymbol{u} = \sum_{\alpha=1}^{2}\sum_{i=1}^{P} f_i^{\alpha}\boldsymbol{e}_i, \tag{24}$$

$$f_i^{\alpha(eq)} = w_i n^\alpha \left[1 + \gamma_i + \boldsymbol{e}_i \cdot (\boldsymbol{u} + \tau \boldsymbol{a}^\alpha) + \tfrac{1}{2}(\boldsymbol{e}_i \cdot (\boldsymbol{u} + \tau \boldsymbol{a}^\alpha))^2 - \frac{(\boldsymbol{u} + \tau \boldsymbol{a}^\alpha) \cdot (\boldsymbol{u} + \tau \boldsymbol{a}^\alpha)}{2}\right] \quad \alpha = 1, 2, \tag{25}$$

where $\gamma_i = 0$, as we have set θ to unity.

The specific force $\boldsymbol{a}^\alpha$ for species α consists of the external specific force $\boldsymbol{a}^\alpha_{ext}$ and that due to inter-particle interactions, $\boldsymbol{a}^\alpha_{int}$:

$$\boldsymbol{a}^\alpha = \boldsymbol{a}^\alpha_{ext} + \boldsymbol{a}^\alpha_{int}. \tag{26}$$

Following Shan & Chen (1993) and Shan & Doolen (1995), we set

$$\boldsymbol{a}^\alpha_{int} = \sum_{\bar{\alpha}=1}^{2} G_{\bar{\alpha}\alpha} \sum_{i=1}^{P} \psi^\alpha(\boldsymbol{x} + \boldsymbol{e}_i) \psi^{\bar{\alpha}}(\boldsymbol{x}) \boldsymbol{e}_i, \tag{27}$$

where ψ^α and $G_{\bar{\alpha}\alpha}$ denote the interaction potential of species α and Green's function, respectively:

$$G_{\bar{\alpha}\alpha}(|\boldsymbol{x} - \boldsymbol{x}'|) = \begin{cases} 0, & |\boldsymbol{x} - \boldsymbol{x}'| > c \\ G_{\bar{\alpha}\alpha}, & |\boldsymbol{x} - \boldsymbol{x}'| = c, \end{cases} \tag{28}$$

where, c, the lattice spacing is equal to $\sqrt{3}$. In all our simulations we use

$$\psi^1 = \sqrt{n^{(1)}\theta - \frac{e_t n^{(1)}}{1 - b n^{(1)}} + a(n^{(1)})^2}, \quad \psi^2 = n^{(2)}, \tag{29}$$

$G_{11} = 2.0$, $G_{12} = G_{21}$ and $G_{22} = 0$. Setting G_{22} to zero is equivalent to requiring that pure species 2 behaves as an ideal gas. The functional form chosen for ψ^1 along with $G_{11} > 0$ implies that pure species 1 obeys a van der Waals equation of state† (Shan & Chen 1993; Shan & Doolen 1995). Repulsive interaction between species 1 and 2, i.e. $G_{12} < 0$, ensures that species 2 will be present predominantly in the gas phase under conditions where gas and liquid containing species 1 and 2 coexist. In the results presented below, we have set $\theta = 1$, $e_t = 1$, $a = 0.45$, and $b = 0.1$.

We performed a number of computational experiments comparing the explicit and implicit LBM schemes. We found that, in every example, the implicit LBM equations could be solved by simple successive substitution in no more than three substitution steps. This added a computational burden of 30% to each time step over that for the explicit scheme. The extra premium is only small because of computationally expensive calculations such as streaming and the 'interparticle' force computation.

4. Phase equilibrium

Consider a system consisting only of pure component 1. As mentioned earlier, this system obeys a van der Waals equation of state. It can be shown readily that the scaled number densities in the bulk gas and liquid phases, which coexist at $\theta = 1$, are 1.09 and 6.93, respectively. The spatial variation of number density across a planar interface was probed via two-dimensional simulations, using both explicit and implicit LBM-BGK schemes. We found that the number density profile could be generated easily using the explicit scheme for $v = 0.5$ (lattice units). When the simulations were repeated for progressively smaller values of v, the scheme always failed when

† Note that Shan & Chen (1993) and Shan & Doolen (1995) use a different discretization of the velocity space (and therefore a slightly different discrete form of the Maxwellian) and use the opposite sign convention for the Green's function, which means that given an interaction potential ψ^α the equation of state derived by these workers differs slightly.

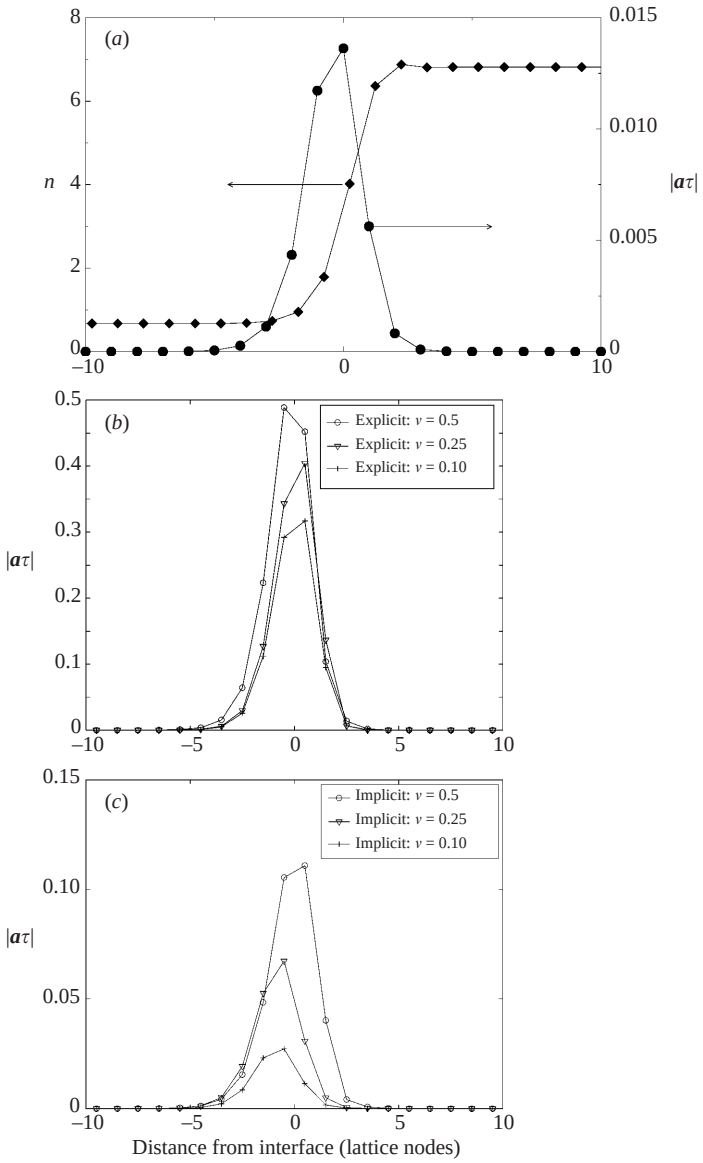

FIGURE 1. (*a*) Variation of n (filled diamonds) and $|\boldsymbol{a}\tau|$ (filled circles) across a planar interface, predicted by the implicit scheme. $v = 0.05$. (*b,c*) Variation of $|\boldsymbol{a}\tau|$ across a planar interface, predicted by (*b*) the explicit scheme and (*c*) the implicit scheme for three different values of v. Simulations were performed in a periodic domain with 50×50 nodes for 10 000 (lattice) time steps to ensure equilibration. Solid lines are drawn to guide the eye.

v was decreased below $v \approx 0.10$. In many of our simulations, it failed even when $v = 0.15$. Close scrutiny of the results revealed that failure of the scheme was always preceded by some of the f_i in the interfacial region becoming negative. In contrast, the implicit scheme continued to converge, yielding only positive values for f_i in all the simulations we performed.

Figure 1(*a*) shows results obtained via the implicit scheme, with $v = 0.05$ (which is a value used in many of our simulations). The implicit scheme gave converged

solutions for v even as small as $v = 0.01$ (which was used in flow simulations at low Morton number, $Mo \approx 10^{-10}$). Figure 1(a) also shows the variation of $|\boldsymbol{a}\tau|$ across the gas–liquid interface in the implicit scheme with $v = 0.05$. The effect of v on the spatial variation of $|\boldsymbol{a}\tau|$ for the explicit and implicit schemes is shown in figures 1(b) and 1(c), respectively.

Since $\tau = 0.5 + v$ in the explicit scheme (for a chosen value of v) while $\tau = v$ in the implicit scheme, one can anticipate $|\boldsymbol{a}\tau|$ to be larger in the case of the explicit method. The derivation of the LBM-BGK method described earlier, be it explicit or implicit, involves the crucial approximation of an exponential by its first two Taylor series terms, resulting in (12). This assumption (that $|\boldsymbol{a}\tau| \ll \theta^{1/2}$), is clearly more accurately satisfied by the implicit scheme for the same v than the explicit one; furthermore, due to its stability, the implicit scheme can be used in small-τ regimes, where the assumption will hold even better.

In either scheme, decreasing v will decrease $|\boldsymbol{a}\tau|$. However, there is a limit on how small $|\boldsymbol{a}\tau|$ can be made in the explicit scheme, as $\tau > \frac{1}{2}$. In contrast, $|\boldsymbol{a}\tau|$ can be made much smaller in the implicit scheme. In all the results presented below, we have applied only the implicit scheme. When the above assumptions hold well for both schemes, and the explicit scheme is stable, we have repeatedly confirmed that the two schemes give essentially identical results.

As mentioned earlier, we have simulated gas–liquid flow using a two-component system. We began by exploring how the choice of the interaction parameter G_{12} influences the manner in which the two components distribute themselves among the gas and liquid phases, and the interfacial tension. Figure 2(a) shows the P, x, y projection for various values of G_{12}. Here, P denotes the pressure; x_1 and y_1 denote the number fractions of species 1 in the bulk liquid and gas phases, respectively. These results were generated through simulations in two-dimensional periodic boxes with 50×50 nodes and planar interfaces. Every simulation was initialized with a planar density map, and the system was allowed to evolve to a state of equilibrium. Increasing the repulsive interaction between the unlike components decreases the number fraction of the volatile component in the liquid phase. The interfacial thicknesses (as number of nodes) calculated using the '10–90' method (Rowlinson & Widom 1982), δ, for various values of G_{12} and x_1 are given in figure 2(b).

As expected, increasing the repulsion decreases the interface thickness. It is clear from this figure that the radius of the bubble in flow simulations should be larger than 3 nodes. In most of our flow simulations the bubble radius was at least 10 nodes, while in a few instances (such as the analysis of bubble coarsening described below) initial bubble radii as small as 6 nodes were used. (It should be mentioned that we did not seek to resolve the gradients in the interfacial regions accurately. Nourgaliev, Dinh & Sehgal (2001) describe alternative schemes which allow one to study the problem of phase separation accurately. In our studies, we sought to maintain a small interfacial thickness so that we could investigate the two-phase hydrodynamics on a larger length scale.)

For the purpose of our computational experiments on bubble motion, the key requirement that we imposed on the phase equilibrium characteristics was that condensation and evaporation should occur at time scales significantly larger than the time scale of the flow problem. Thus, for example, we ensured that phenomena such as bubble coarsening, in which large bubbles grew at the expense of smaller bubbles, did not occur to a significant level during the course of our flow simulations. This was achieved by choosing a sufficiently strong interspecies repulsion parameter. Typical computational time in our flow simulations was 10^4 (lattice units). Therefore, we

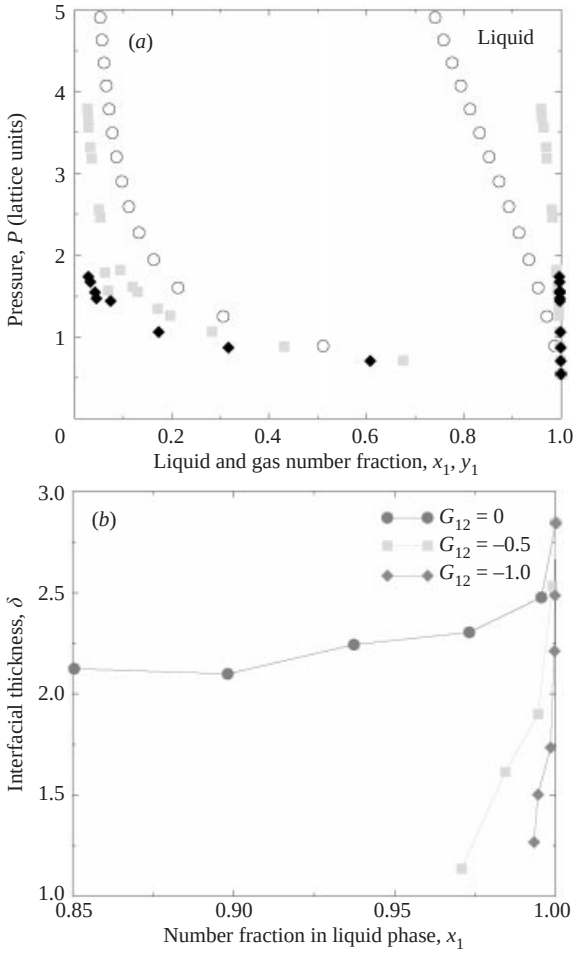

FIGURE 2. (*a*) P, x, y projection of phase behaviour at different interspecies repulsion levels. For all simulations $G_{11} = 2$ and $G_{22} = 0$. ○, $G_{12} = 0$; ■, $G_{12} = -0.5$; ◆, $G_{12} = -1.0$. (*b*) Interface thickness, δ, as a function of G_{12} and liquid composition, x_1. Solid lines are drawn to guide the eye.

demanded that the bubble coarsening time was significantly larger than 10^4. In order to obtain an estimate for the bubble coarsening time, the following two-dimensional simulations were performed using $v = 0.1$: two gas bubbles of radii 6 and 10 lattice nodes were allowed to equilibrate separately in 50×50 periodic boxes. They were then juxtaposed creating a 100×50 periodic box, and were allowed to re-equilibrate. Through bubble coarsening, the smaller bubble slowly dissolved while the larger one grew in size. The bubble coarsening time was defined as the time necessary for the smaller bubble to dissolve completely. Figure 3 shows the effect of G_{12} on the bubble coarsening time. It can be seen from this figure that $G_{12} = -1.0$ was an adequate level of interspecies repulsion for our computational experiments on bubble motion.

Figure 4 shows the effect of G_{12} on interfacial tension, σ. In order to compute σ, two-dimensional simulations were performed in 50×50 periodic boxes where a single bubble was allowed to equilibrate. The value of σ was then extracted from the gas- and liquid-phase pressures and bubble size, using Laplace's law. The validity of this approach to determine interfacial tension in LBM simulations has been discussed previously in the literature (e.g. Shan & Chen 1993; Huo *et al.* 1997). It is clear from

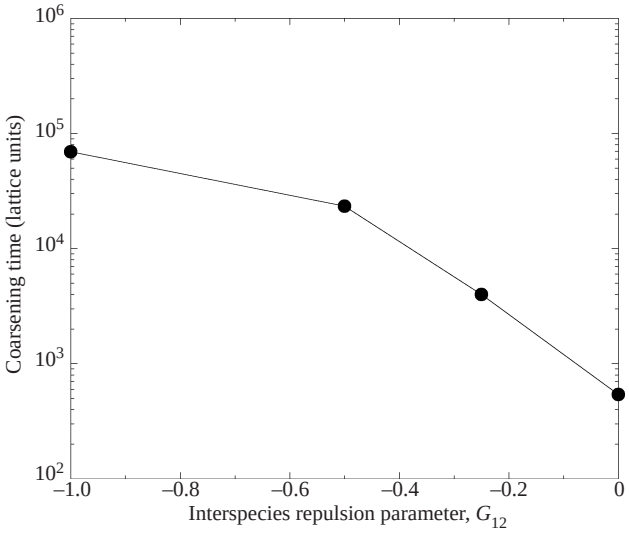

FIGURE 3. Coarsening time (see text) vs. interspecies repulsion parameter G_{12}. Solid lines are drawn to guide the eye.

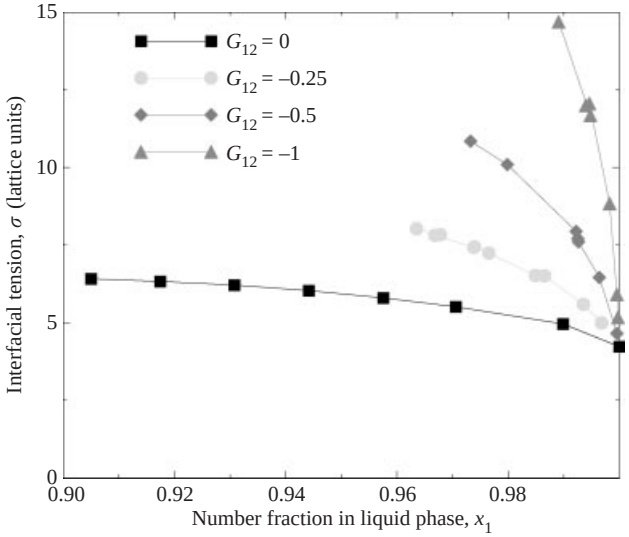

FIGURE 4. Interfacial tension, σ, as a function of G_{12} and liquid composition, x_1. Solid lines drawn to guide the eye.

this figure that our choice of equation of state restricts the value of σ to lie in a narrow window. This window is even narrower (namely 4 to 9 lattice units) if we further demand that the liquid phase be almost completely pure component 1.

5. Bubble rise results

5.1. *Rise velocity of essentially isolated three-dimensional bubbles*

We began by considering the motion of a bubble in a periodic box, choosing the box size to be much larger than the bubble. A two-component system with $G_{12} = -1.0$ was

used in these calculations. In addition to $\boldsymbol{a}_{int}$, which gave rise to the phase separation, an external specific force was introduced causing the bubbles to rise:

$$\boldsymbol{a}_{ext}^{(1)} = \boldsymbol{a}_{ext}^{(2)} = \boldsymbol{a}_{ext} = \boldsymbol{g}\left(1 - \frac{\langle n\rangle}{n}\right), \tag{30}$$

where n is the mixture number density at the node of interest and $\langle n\rangle$ is the average number density of the mixture in the entire periodic domain. This choice ensured that the average value of $n\boldsymbol{a}_{ext}$ in the periodic domain was zero, so that the mass-average velocity of the mixture in the box remained independent of time. In all our simulations, the initial mass-average velocity of the mixture in the periodic box was zero. Then, as the gas bubble rose, the surrounding liquid acquired a small downward velocity.

Since we do not model the system as immiscible phases, but through coexisting phases from an equation of state, both flow and mass transport between phases occur simultaneously. It is not practically possible to prescribe the number density in the bulk liquid, n_ℓ (and in the bulk gas, n_g) *a priori*. What we can prescribe, are the domain averages $\langle n^{(1)}\rangle$ and $\langle n^{(2)}\rangle$. Through these we can alter the volume of gas in the bubble and hence, d_e, the effective bubble size. When this is done, the bulk liquid (gas) composition evolves to equilibrium; while one can more or less predict the expected equilibrium values, small adjustments are inevitable, and they also cause a corresponding change in σ. However, these changes were small and the values of σ and n_ℓ stayed close to 4 and 7 lattice units, respectively. Given this, we had limited options to achieve small Morton numbers ($Mo \approx 10^{-10}$) and Eötvös numbers (Eo) of order unity. As

$$\frac{Mo}{Eo} = \frac{n_\ell^2 v^4}{\sigma^2 d_e^2}, \tag{31}$$

achieving $Mo/Eo \approx 10^{-10}$ requires $v^2/d_e \approx 10^{-5}$ lattice units. Setting $v \approx 0.2$ (which was the lowest value we could consistently assign to v in the explicit scheme, without causing the scheme to fail), we conclude that the $d_e \approx 4 \times 10^3$ for $Mo/Eo \approx 10^{-10}$. In contrast, in the implicit scheme, we could easily carry out simulations with $v = 0.01$ thus lowering the bubble size by a factor of 400 (when compared to the explicit scheme). This highlights the advantage of the implicit scheme.

The rise velocities of essentially isolated bubbles at various Mo and Eo were calculated as follows: an initial density map satisfying the desired $\langle n^{(1)}\rangle$ and $\langle n^{(2)}\rangle$ was set up in a three-dimensional periodic box, and the system was allowed to equilibrate in the absence of gravity. This produced a spherical bubble. The bulk liquid and gas densities were then determined from the simulation results. Using these and the known domain-average mixture density, we computed ϕ, and d_e through $\phi = (\rho_l - \bar{\rho})/(\rho_l - \rho_g)$ and $d_e = (6\phi V/\pi)^{1/3}$, with V the volume of the computational box. (The definition of d_e changes in an obvious manner for two-dimensional simulations.) It is clearly reasonable to identify ϕ with the volume fraction (three dimensions) or area fraction (two dimensions) of the bubble and d_e with the equivalent bubble diameter. We found this method for finding ϕ and d_e to be computationally convenient. We have verified that ϕ found in this manner differs by less than 0.1% from the value computed using a cut-off function to separate gas and liquid phases.

We then turned on gravity, causing the bubble to rise, and computed the volume-average velocity of the mixture in the computational domain as a function of time. From a knowledge of bubble volume (area) fraction, volume-average velocity of the mixture and the fact that the mass-average velocity of the mixture in the domain

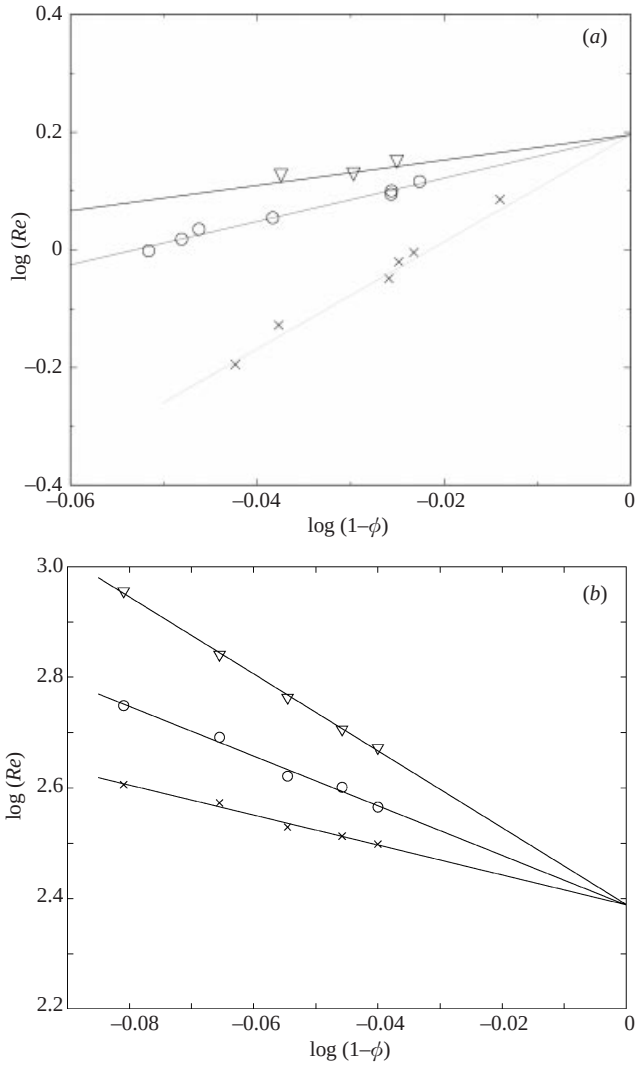

FIGURE 5. Dimensionless bubble rise velocity as a function of bubble volume fraction, ϕ. Single bubble in a periodic box. (*a*) $Mo = 8.6 \times 10^{-5}$, $Eo = 0.38$. Essentially spherical bubble. Aspect ratios of the box are as follows: ∇, 1.5:1.5:1; where the last direction denotes the rise direction; $\circ$, 1:1:1; $\times$, 1:1:1.5. (*b*) $Mo = 10^{-7}$, $Eo = 9.1$, Spherical cap bubble. Aspect ratios of the box are as follows: ∇, 1.2:1.2:1; $\circ$, 1:1:1; $\times$, 1:1:1.2.

was zero, we calculated the domain-average velocities of the gas and liquid phases at each instant of time. (The bubble fraction ϕ changed only in the fourth significant digit, after turning on gravity and establishing flow.) We define slip velocity ($\boldsymbol{v}$) as the difference between domain-average gas and liquid velocities. Transient integration was continued until a steady slip velocity was obtained. In cases where the slip velocity manifested a periodic variation, integration was carried out for a long enough duration to compute the mean value.

Such calculations were repeated for various bubble volume fractions (by choosing larger and larger periodic boxes and a fixed bubble size), in order to compute slip velocity as a function of bubble volume fraction, ϕ. By extrapolating the results to

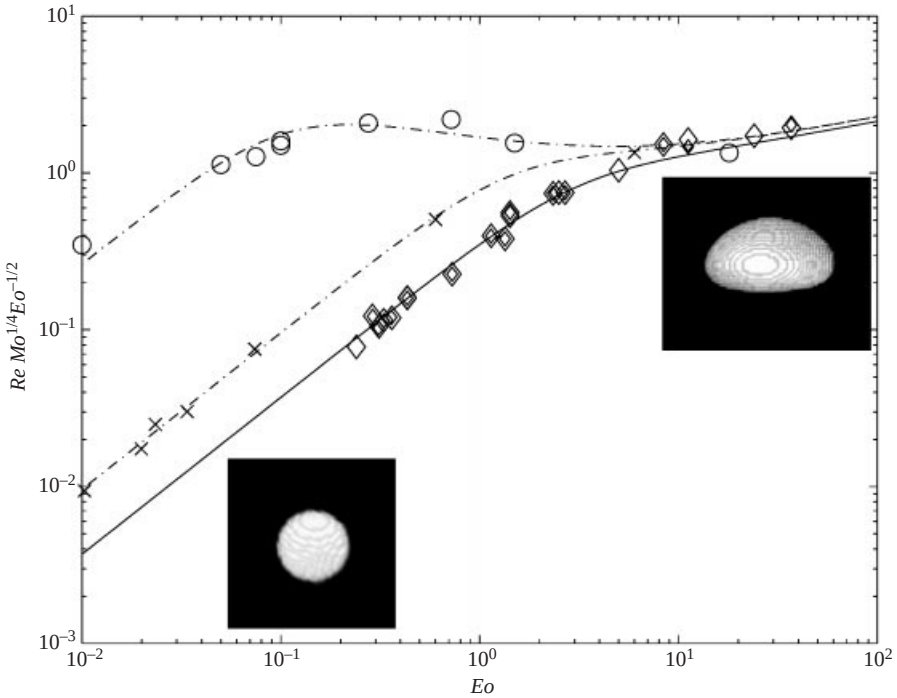

FIGURE 6. Single-bubble rise velocity ($Re_\infty Mo^{1/4}Eo^{-1/2} = v(\rho_l/\sigma_g)^{1/4}$) vs. the Eötvös number for various Morton numbers. The solid lines denote a correlation due to Fan & Tsuchiya (1990), and the symbols denote the LBM results: ×, $Mo = 1.5 \times 10^{-5}$; ◇, $Mo = 7.8 \times 10^{-4}$; ○, $Mo = 3.9 \times 10^{-10}$.

$\phi \to 0$, single bubble rise velocities were estimated. In general, at any given ϕ, the slip velocity depended on the assumed aspect ratio of the periodic box. However, extrapolation to $\phi = 0$ consistently yielded essentially the same slip velocity for isolated bubbles for a range of box aspect ratios. This is illustrated in figures 5(a) and 5(b) for nearly spherical and highly distorted bubbles, respectively.

Figure 6 shows rise velocities of essentially isolated bubbles (Re_∞) computed in this manner, for various Eo and Mo. Also shown in this figure is an empirical correlation due to Fan & Tsuchiya (1990):

$$Re\,Mo^{1/4}Eo^{-1/2} = \left[\left(\frac{Mo^{-1/4}Eo}{K_b}\right)^{-N} + \left(\frac{2C}{Eo^{1/2}} + \frac{Eo^{1/2}}{2}\right)^{-N/2}\right]^{-1/N}, \qquad (32)$$

where N is an empirical parameter introduced to accommodate both purified and contaminated systems. The recommended value of N ranges between 0.8 (clean) and 1.6 (contaminated) depending on the liquid purity. It is recommended to use $C = 1.2$ and 1.4 for monocomponent and multicomponent liquids, respectively. The value of K_b is correlated as $K_b = K_{b0}Mo^{-0.038}$, where $K_{b0} = 14.7$ and 10.2 for aqueous solutions (or water) and organic solvents/mixtures, respectively. If K_b is computed to be less than 12, the value of 12 should be used. In our work, we have used the value of $N = 0.8$, $C = 1.2$ and $K_{b0} = 10.2$.

The insets in figure 6 show typical shapes of bubbles at low and high Eo, respectively. The good agreement between LBM predictions and the correlation lends credibility to the use of the scheme to this class of problems.

Re	F_∞	Aspect ratio	*We*
110	2.12	0.95	0.38
161	1.25	0.9	0.69
200	−2.45	0.82	1.39
345	−36.5	0.7	2.5

TABLE 1. Effect of bubble deformation on rise velocity.

5.2. *Aspect ratio of bubbles and wake characteristics*

The importance of the shape deformation on the rise velocity of bubbles can be established by comparing the results obtained in our study with those reported by Yuan & Prosperetti (1994) for spherical bubbles. These authors examined the buoyant rise of two equal-sized spherical bubbles moving along their line of centres by solving the full Navier–Stokes equations using a mixed spectral/finite-difference scheme for Reynolds numbers up to 200. Free-slip conditions were imposed at the bubble surfaces, while the normal stress condition was replaced by a sphericity constraint under the assumption of a small Weber number. They found that the drag coefficient C_D of the two bubbles could be represented as (Moore 1963)

$$C_D = \frac{48}{Re}\left(1 - \frac{F(x)}{Re^{1/2}}\right), \tag{33}$$

where x denotes the separation of the bubbles. Here the function F is different for the leading and trailing bubbles, but in the limit of large separation, both were found to reach the same asymptote of 2.221. This result is shown in figure 7 as a broken line. The solid line in this figure corresponds to equation (32) and $Mo = 3.9 \times 10^{-10}$. The points refer to the single-bubble limits obtained in our LBM results. The insets show the density maps for various bubbles (obtained in simulations at bubble volume fractions less than 0.03) so that the shape deformation can be seen clearly. Table 1 summarizes the *Re* and *We* values and the bubble aspect ratios (h/D) extracted from our simulations, where we have also shown the values of $F_\infty (= F(x \to \infty))$ which will be needed to fit each of the data points. It is readily apparent that the value of F_∞ decreases as *We* increases. As *We* increases, the bubble deformation increases, and the spherical bubble approximation is valid for only small *We*, as one would indeed expect. The results in table 1 could be captured as $h/d = 1 - 0.12We$.

A typical benchmark calculation in the analysis of bubble rise behaviour is the computation of the wake velocity profile in the horizontal plane which contains the stagnation point, see figure 8. Also shown in this figure are curves representing different flow models of a spherical vortex. The trend predicted by LBM is reasonable.

Figure 9 presents the effect of bubble fraction on the aspect ratio of ellipsoidal bubbles determined from LBM simulations for $Eo = 3.1$ and $Mo = 10^{-7}$. The solid line in this figure shows the prediction of a potential flow theory by Moore (1959). The simple theory of Moore (1959) and the LBM results show the same trend. Quantitative agreement should not be expected as the simulations include viscous effects, which were not considered by Moore (1959).

In what follows, the word 'streamlines' denotes the output of Matlab generating software using the velocity field in the comoving frame. While these images make sense only for incompressible flow, we still find them to be a useful method of visualizing the flow field, and so we report them, apologizing for the abuse of terminology.

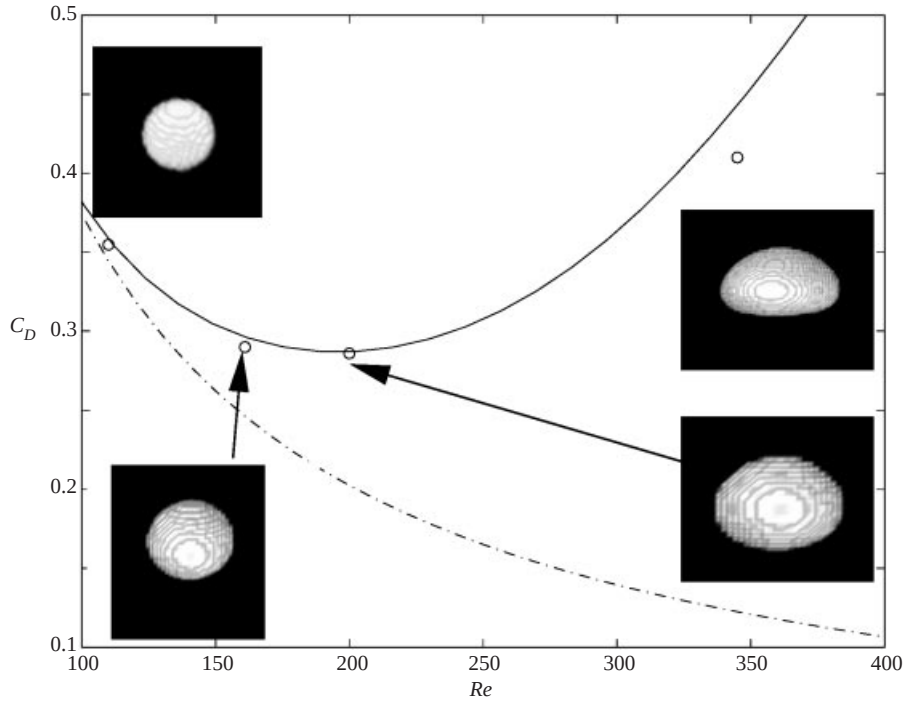

FIGURE 7. The drag coefficient of isolated bubbles at various Reynolds numbers. ——, Fan & Tsuchiya (1990) with $Mo = 3.9 \times 10^{-10}$. — — —, equation (33) with $F = 2.221$. ○, Single bubble limits of our three-dimensional LBM simulations. Simulations were performed using between $50 \times 50 \times 50$ and $150 \times 150 \times 150$ nodes. Insets show density maps to highlight the extent of bubble deformation.

'Streamlines' for the case of a steadily rising circular cap bubble in a square periodic box at a low bubble fraction is shown in figure 10. The presence of a closed wake is clearly evident, and the bubble is clearly separated from the wake of the preceding bubble. Nevertheless, it is clear from figure 9 that the aspect ratio of a bubble is affected by bubble–bubble interactions even at such low bubble fractions. Hence aspect ratios of essentially isolated circular or spherical cap bubbles can be computed only through simulations at much smaller bubble volume fractions. When this simulation was repeated at twice the resolution using 200 × 200 grids, Re increased slightly to 75.9. We performed similar calculations for several different Eo and Mo values, probing the effect of grid resolution on the rise velocities, and made sure that the rise velocities presented in this paper (and the virtual mass coefficients discussed later) are essentially independent of grid resolution.

We attempted to investigate the extent to which the details of the boundary layer near a high Reynolds number bubble could be resolved by the lattice Boltzmann scheme. As noted earlier, the gas–liquid interface assumes a finite thickness in this numerical scheme and the presence of such a diffuse interface made it difficult to state with any degree of confidence whether the boundary layer was resolved in any of the simulations involving high Reynolds number bubbles. At the same time, our simulations do suggest that the bubble rise velocity and the virtual mass coefficient can indeed be computed rather accurately.

The aspect ratios of two- and three-dimensional bubbles for various combinations of Eo and Mo (and at very low bubble fraction), were determined through LBM

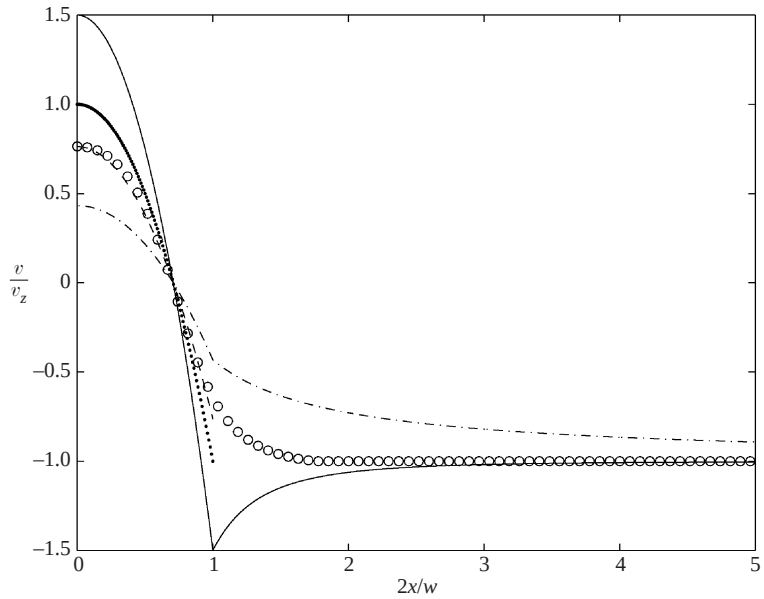

FIGURE 8. Scaled wake velocity in the horizontal plane passing through the centre of a standing vortex ring in the wake of a spherical cap bubble ($Eo = 10$, $Re = 50$, $Mo = 10^{-4}$). ○, LBM; ——, Hill's spherical vortex (1894); — — —, Harper–Moore (1968); · · · ·, Parlange (1970); — · — · —, Hadamard–Rybczynski creeping flow vortex (Leal 1992). LBM simulations were done in a $100 \times 100 \times 50$ periodic box, where the last number denotes the rise direction. The combined volume fraction of the bubble and wake was roughly 0.01. v is bubble rise velocity, v_z is velocity in the rise direction, w is wake width in this plane, x denotes radial distance measured from the z-axis of symmetry.

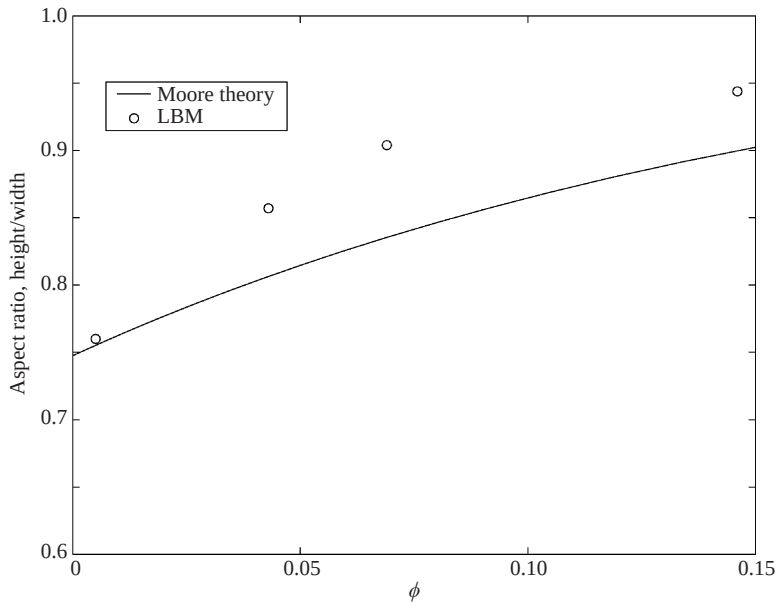

FIGURE 9. Aspect ratio of a three-dimensional bubble as a function of bubble volume fraction. $Eo = 3.1$, $Mo = 10^{-7}$, $Re_\infty = 180$. Single bubble in a periodic box. $50 \times 50 \times 50$ to $80 \times 80 \times 80$ nodes. Gravity pointing in $-z$-direction. Solid line: Moore (1959).

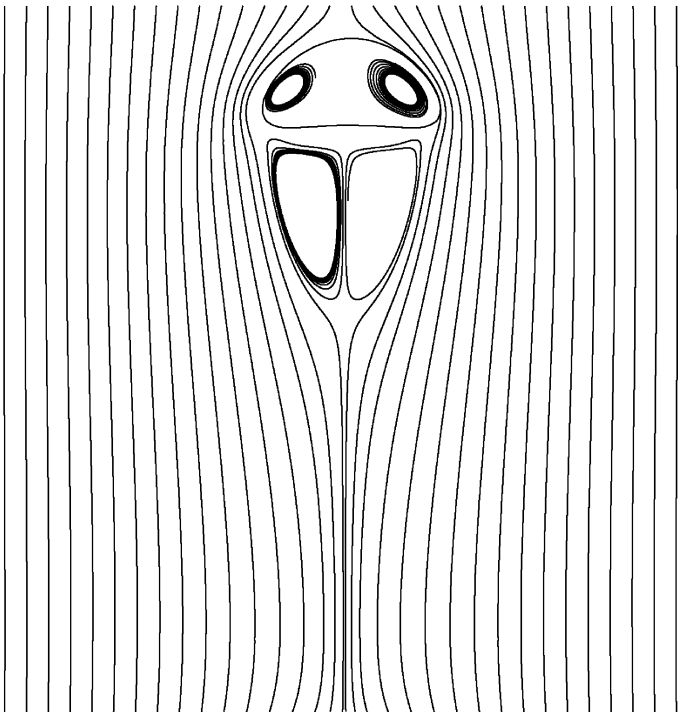

FIGURE 10. 'Streamlines' for bubble rise at bubble area fraction of 0.0375 showing a closed wake. 100×100 nodes. Gravity pointing in $-y$-direction. $Mo = 10^{-5}$, $Eo = 1.2$. $Re = 75.2$.

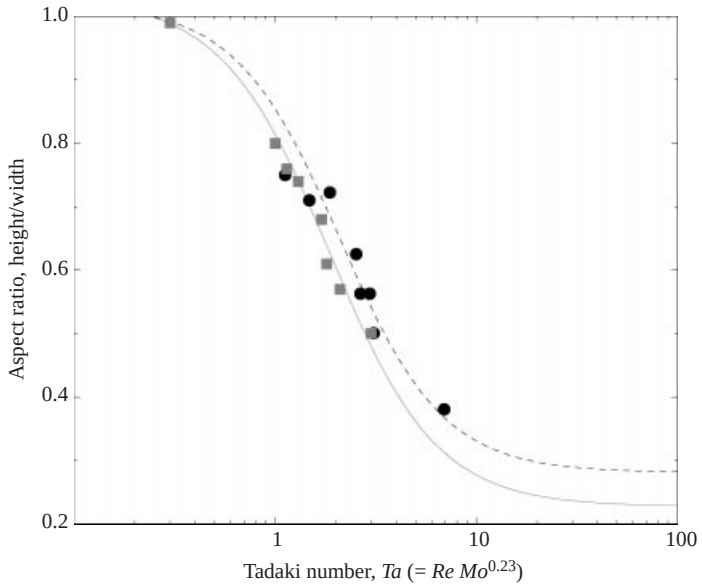

FIGURE 11. Bubble aspect ratio vs. Tadaki number ($Ta = Re\,Mo^{0.23}$). Vakhrushev–Efremov (1970) correlation for three (solid line) and two dimensions (dotted line); ■, three-dimensional LBM; ●, two-dimensional LBM. Simulations were done in $80 \times 80 \times 80$ (three-dimensional) and 80×80 (two-dimensional) periodic domains. $1 < Eo < 10$ and $10^{-4} < Mo < 10^{-8}$. Bubble volume or area fraction in every one of these simulations is less than 0.02.

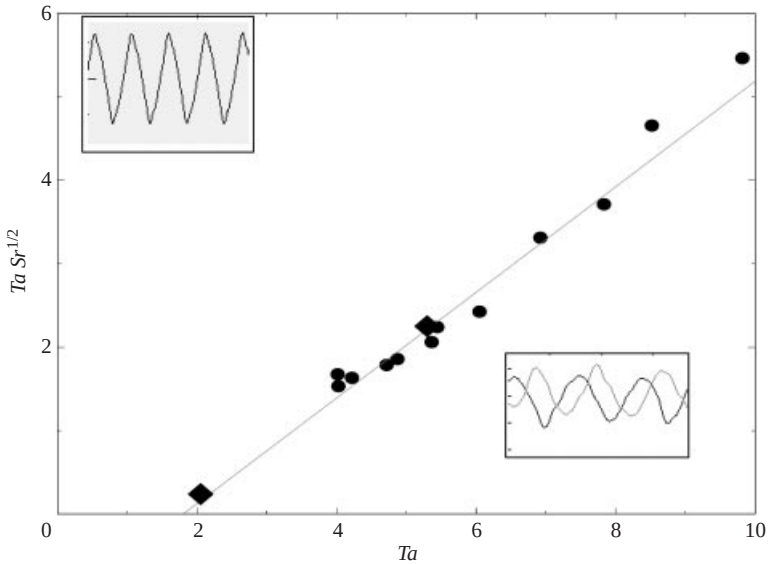

FIGURE 12. Comparison of LBM results for wake shedding frequency with correlation given in Fan & Tsuchiya (1990) (solid line). ◆, three-dimensional; ●, two-dimensional, $1 < Eo < 10$ and $10^{-4} < Mo < 10^{-8}$. Insets: sample results of two-dimensional and three-dimensional run showing periodicity in slip velocity. Top left inset (two-dimensional): typical x velocity vs. time (rise in y-direction). Bottom right inset (three-dimensional) typical x and y velocity vs. time (rise in z-direction). The bubble fraction is between 2 to 3%.

simulations. Figure 11 shows the variation of aspect ratio with the Tadaki number, $Ta = Re_\infty Mo^{0.23}$ (Clift, Grace & Weber 1978; Fan & Tsuchiya 1990). Also shown in this figure are the correlations described by Fan & Tsuchiya (1990). The functional form of this correlation was originally proposed by Vakhrushev & Efremov (1970) (cited in Fan & Tsuchiya 1990) and the adjustable constants were determined by Fan & Tsuchiya (1990). The agreement is encouraging.

When $Ta \approx 2$, the bubbles rise in an oscillatory manner, and we computed the frequency of this oscillation and the corresponding Strouhal number ($Sr = fd_e/v$) for both two- and three-dimensional simulations. Fan & Tsuchiya (1990) noted that experimental data on wake shedding frequencies could be captured by $TaSr^{1/2} = 0.632(Ta - 1.8)$. Figure 12 shows the remarkable agreement between the LBM predictions and the correlation.

Figure 13 shows the streamlines for the same combination of Eo and Mo as in figure 10, but for a larger bubble fraction. The bubble now interacts strongly with the wake of the preceding bubble. This is accompanied by a stretching of the bubble in the vertical direction and an increase in the aspect ratio.

The same effect is seen in three-dimensional simulations as well, and this is illustrated in figure 14. The aspect ratio of the spherical cap bubble changes dramatically with bubble fraction.

5.3. *Effect of bubble volume fraction on rise velocity of periodic arrays of bubbles (three-dimensional)*

We simulated the rise behaviour of isolated bubbles in cubic periodic boxes of various sizes to explore the effect of bubble volume fraction (ϕ) on the effective rise velocity of cubic arrays of bubbles at various Eo and Mo values. Figure 15 shows the effect

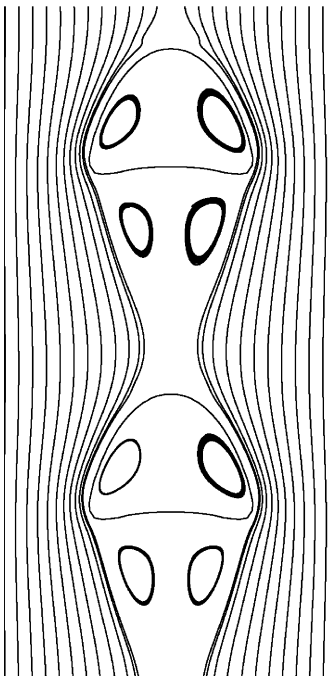

FIGURE 13. 'Streamlines' for bubble rise at bubble area fraction of 0.15 showing a closed wake. 50×50 nodes. Two periodic boxes. Gravity pointing in $-y$-direction. $Mo = 10^{-5}$, $Eo = 1.2$. Interaction between bubble and the wake of the preceding bubble tends to stretch the bubble in the y-direction.

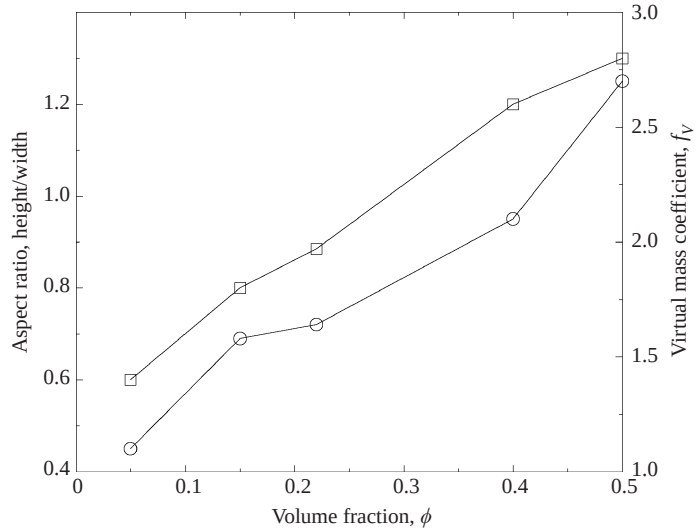

FIGURE 14. Aspect ratio (○) and virtual mass (□) of a three-dimensional bubble as a function of bubble volume fraction. $Eo = 12$, Mo $= 10^{-7}$, $Re_\infty = 250$. Lines are drawn to guide the eye.

of ϕ on the dimensionless rise velocity, expressed as a Reynolds number, for several values of Eo and $Mo = 7.2 \times 10^{-4}$. In all cases the effect of bubble fraction could be captured through a Richardson–Zaki (1954) relation $Re = Re_\infty(1-\phi)^{n-1}$. It is clear from figure 15 that, as Eo increased, the R–Z exponent, n, decreased. When $n > 1$,

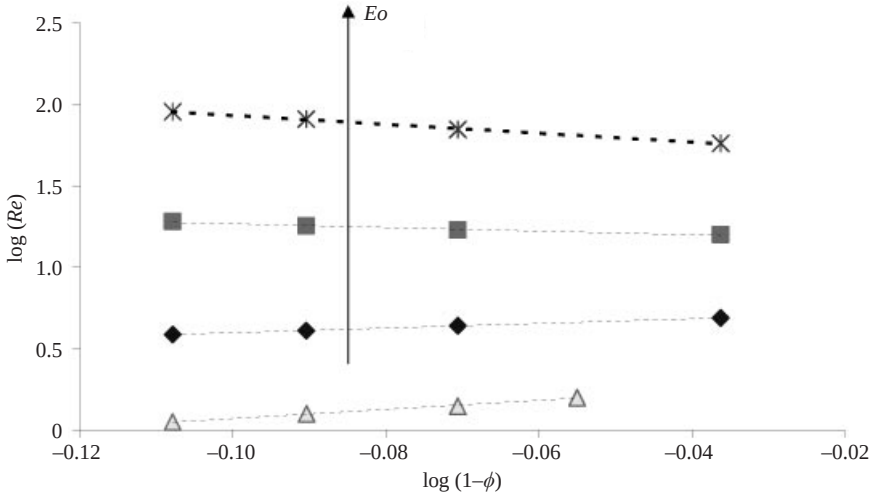

FIGURE 15. Rise velocity for a $Mo = 7.2 \times 10^{-4}$ system at various Eo and bubble volume fractions, ϕ in three-dimensions. Single bubble in a cubic box.

the assembly of bubbles rises more slowly than an isolated bubble. In contrast, $n < 1$ represents a cooperative rise of bubbles in the assembly. It can be seen from figure 15 that such a cooperative rise of bubbles occurs at sufficiently large values of Eo.

This is seen more clearly in figure 16(a), where the R–Z exponents obtained for various combinations of Eo and Mo are plotted in the usual n vs. Re_∞ format. The solid line in this figure is the relationship determined by Richardson & Zaki (1954) from their experiments on hindered sedimentation of solid particles in liquids. Our results agreed with the R–Z line for $Re_\infty < Re^*$, where Re^* is a function of Mo. When $Re_\infty > Re^*$, the computed values of the exponent n decreased rapidly with Re_∞. Visual inspection of the density maps clearly showed that $Re_\infty \sim Re^*$ corresponded to a condition when the bubbles began to deform appreciably and assumed an ellipsoidal shape. Further increase in Re_∞ led to spherical cap bubbles. The cooperative rise behaviour (namely, $n < 1$) may be rationalized as follows. At small bubble fraction (ϕ), the acceleration of the liquid as it flows past the sides of the bubble produces a suction at the sides, which leads to an oblate bubble shape (as in figure 10). In a periodic array, as the bubble fraction increases, the wake occupies a larger and larger fraction of the volume and eventually spans the region from one bubble to the next (as in figure 13). This suggests that the extent to which the liquid outside the wake accelerates and decelerates as it goes past a bubble decreases as ϕ increases. This leads to a progressive decrease in the suction produced at the sides of the bubble as ϕ increases, and the aspect ratio increases toward unity (for example, see figure 9). This in turn increases the rise velocity of the bubbles.

Note that the aspect ratio can exceed unity (see figure 14), which suggests that a direct interaction between a bubble and the wake of the preceding bubble may also be present, where a bubble is being pulled upward by the wake of the preceding bubble. Such a suction may also contribute to cooperative rise. Wilkinson, Spek & van Dierendonck (1992) and Krishna *et al.* (1999) refer to this wake effect as an acceleration factor. Unfortunately, there is no simple way of comparing our results with their correlations.

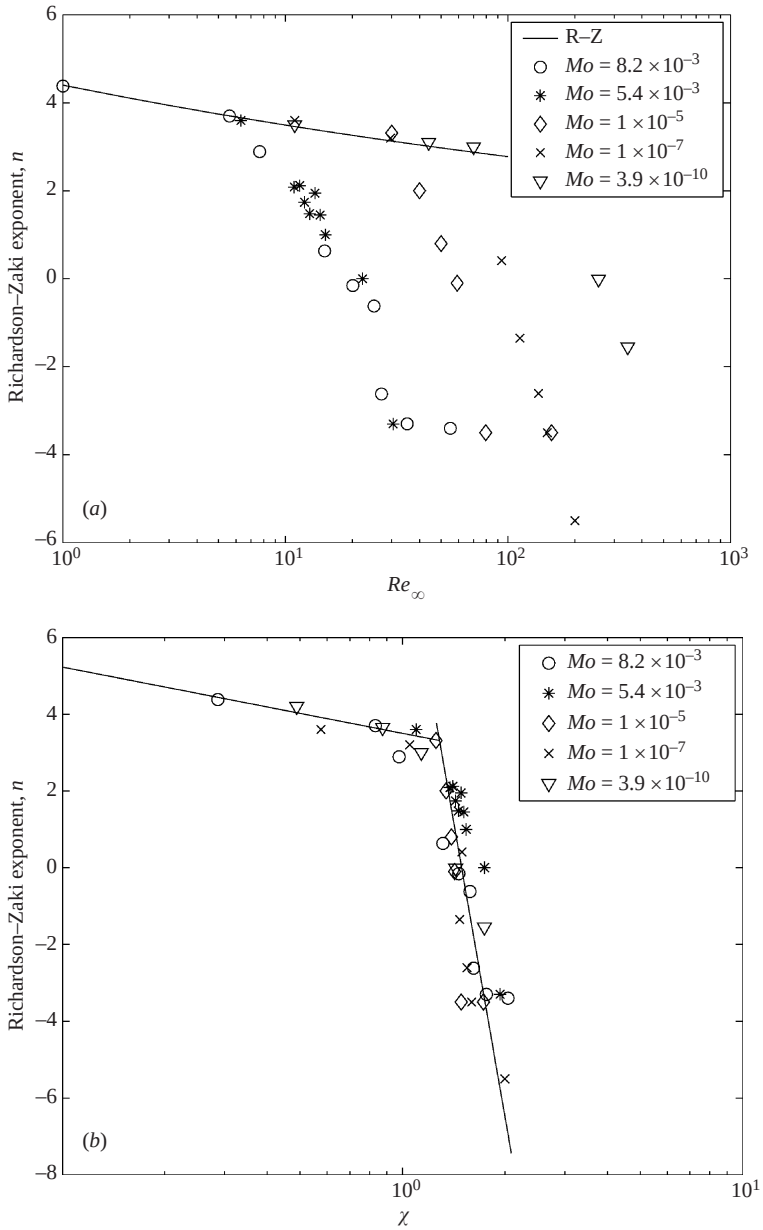

FIGURE 16. (*a*) Richardson–Zaki exponent, n, as a function of Mo and Re_∞. The solid line denotes the R–Z exponent as a function of Re_∞, as suggested by Richardson & Zaki (1954). (*b*) Richardson–Zaki exponent, n, as a function of $\chi = Re_\infty Mo^{1/4} Eo^{-1/2}$. Solid lines: see equation (34).

The results obtained with systems having a high Mo (see open circles and diamonds in figure 16*a*) suggested that there may be large-Re_∞ asymptotes for the exponent n. Simulations at $Mo = 10^{-7}$, however, did not corroborate the existence of such an asymptote. In figure 16(*b*), we have replotted the data in figure 16(*a*) to show that the results of figure 16(*a*) could be collapsed approximately into a single master curve. The abscissa in figure 16(*b*) is same as the ordinate in figure 6. The lines in

figure 16(*b*) correspond to

$$n = \begin{cases} 3.3 - 1.7\log(\chi/1.3), & \chi < 1.3 \\ 3.3 - 51\log(\chi/1.3), & \chi \geqslant 1.3, \end{cases} \tag{34}$$

where $\chi = Re_\infty Mo^{1/4} Eo^{-1/2}$, and this may be used as a computationally generated closure for n.

A closure for the interphase drag force, $\boldsymbol{F}_D$ to be used as one of the contributors to $\boldsymbol{F}$ in (3) and (4), may now be written as follows:

$$\boldsymbol{F}_D = -\beta(\phi)(\boldsymbol{u}_g - \boldsymbol{u}_l), \tag{35}$$

with

$$\beta(\phi) = \frac{\Delta\rho g\phi}{v_t(1-\phi)^{n-2}} = \frac{\Delta\rho g d_e \phi}{\nu Re_\infty (1-\phi)^{n-2}}, \tag{36}$$

where v_t is the terminal rise velocity of an isolated bubble and n is the R–Z exponent. The Fan & Tsuchiya (1990) correlation, which captures both the experimental and computationally generated data on rise velocities, or other similar correlations, may be used to find Re_∞ for a specified Eo and Mo in a system with uniformly sized bubbles, while n follows from (34). Clearly, such a closure is limited to $|\boldsymbol{u}_g - \boldsymbol{u}_l|$ not too different from v_t and $0 < \phi < 0.2$. More importantly, it is restricted to cubic arrays of bubbles.

6. Virtual mass coefficient calculations

The virtual mass force per unit volume of the mixture, $\boldsymbol{F}_V$, associated with the acceleration of the bubble phase relative to the surrounding continuous phase, is usually written as (e.g. Felderhof 1991; Zhang & Prosperetti 1994; Spelt & Sangani 1998)

$$\boldsymbol{F}_V = -\rho_l \phi(1-\phi)\left[\frac{\partial \boldsymbol{u}_g f_V}{\partial t} + \boldsymbol{u}_g \cdot \nabla \boldsymbol{u}_g f_V - \frac{\partial \boldsymbol{u}_l f_V}{\partial t} - \boldsymbol{u}_l \cdot \nabla \boldsymbol{u}_l f_V\right], \tag{37}$$

where f_V is the virtual mass coefficient. A well-known result from the application of potential flow theory to flow around spherical (three-dimensional) and circular (two-dimensional) bubbles is that f_{V0} is equal to 0.5 in three dimensions and 1.0 in two dimensions (Auton *et al.* 1988; Lamb 1932). Here, f_{V0} denotes $f_V(\phi \to 0)$. The ϕ-dependence of f_V in the limit of potential flow has been examined by several researchers (Lamb 1932; Zuber 1964; van Wijngaarden 1976; Auton *et al.* 1988; Biesheuvel & Spoelstra 1989; Felderhof 1991; Spelt & Sangani 1998).

Consider a uniform assembly of bubbles at a bubble fraction ϕ, subjected to a steady specific gravity force, $\boldsymbol{g}_0$. The average pressure gradient in the liquid in this state is given by $\nabla P_l = \bar{\rho}\boldsymbol{g}_0$, and the swarm of bubbles will translate at a steady velocity, $\boldsymbol{v}_0$, relative to the surrounding liquid. It follows from (3) and (35) that $\boldsymbol{v}_0 = \boldsymbol{u}_{g0} - \boldsymbol{u}_{l0} = -\phi(1-\phi)\Delta\rho\boldsymbol{g}_0/\beta(\phi)$ where $\boldsymbol{u}_{g0}$ and $\boldsymbol{u}_{l0}$ are the local average velocities of the gas and liquid phases, respectively.

At $t = 0$, we initiate a slow, linear ramp of $\boldsymbol{g}$, $\boldsymbol{g}(t) = \boldsymbol{g}_0(1 + \Psi t)$, set $\nabla P_l = \bar{\rho}\boldsymbol{g}(t)$ and demand that the assembly of bubbles continue to remain spatially uniform. It then follows that the mass-average velocity of the mixture will remain independent of time, while both $\boldsymbol{u}_g$ and $\boldsymbol{u}_l$ will evolve with time. Letting $\boldsymbol{F} = \boldsymbol{F}_D + \boldsymbol{F}_V$, where $\boldsymbol{F}_D$ and $\boldsymbol{F}_V$ are given by (35) and (37), and integrating (3) and (4) we find that the slip velocity increases with time, as sketched in figure 17(*a*), and manifests a linear growth region at large times (provided $\Psi t \ll 1$). (If the Basset force (Basset 1888)

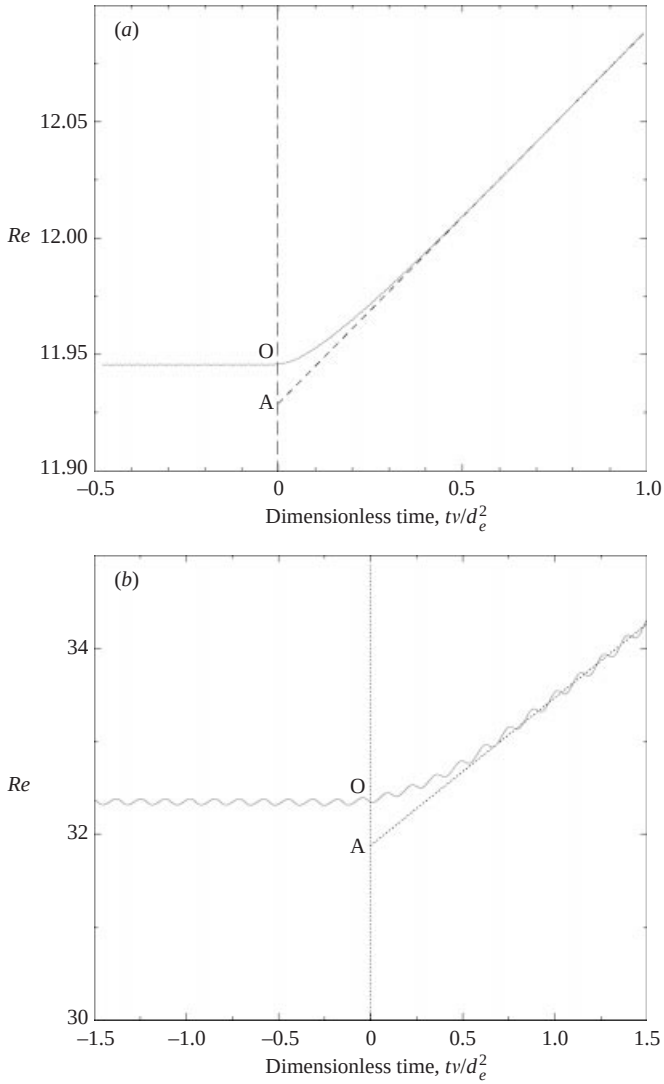

FIGURE 17. (*a*) Sample results for a virtual mass calculation of an essentially circular bubble in two-dimensions. Results for distorted bubbles with steady wakes are similar. Bubble area fraction $\phi = 0.10$, $Eo = 0.85$, $Mo = 3 \times 10^{-4}$, $\Psi d_e^2/\nu = 10^{-2}$. (*b*) Sample results for a virtual mass calculation of a bubble with an oscillating wake. Bubble area fraction $\phi = 0.10$, $Eo = 3.2$, $Mo = 2 \times 10^{-8}$, $\Psi d_e^2/\nu = 10^{-1}$.

is significant, then such a linear variation of the slip velocity with time will not be realized.) It is a straightforward exercise to extract the virtual mass coefficient from the y-intercept (OA) shown in figure 17(*a*).

Such a computational experiment is easily performed using LBM. Figure 17(*a*) shows a typical result obtained with an essentially circular bubble in a two-dimensional periodic box. Similar results are obtained with distorted bubbles with steady wakes. Figure 17(*b*) illustrates a case of a distorted bubble with a shedding wake (in a two-dimensional periodic box).

The effect of ϕ on f_V obtained for spherical and circular bubble is shown in figure 18. Simulations were performed using a single bubble in square or cubic boxes.

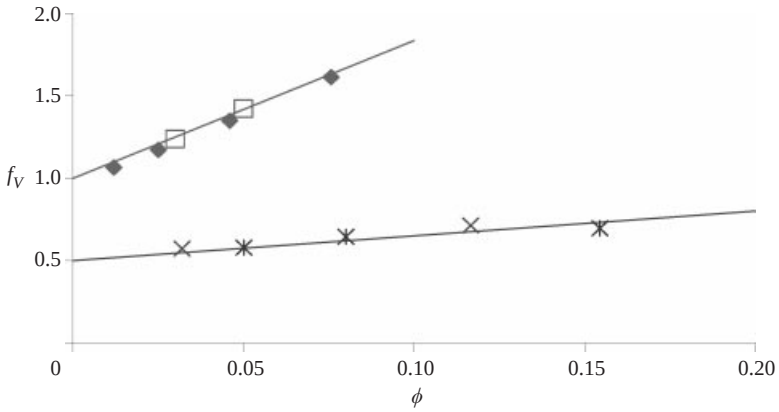

FIGURE 18. Virtual mass coefficients for essentially circular and spherical bubbles vs. bubble volume or area fraction, ϕ. Two dimensions (◆, $Eo = 0.7$, $Mo = 7.19 \times 10^{-4}$, $Re_\infty = 2$; □, $Eo = 0.1$, $Mo = 3.9 \times 10^{-10}$, $Re_\infty = 120$), three dimensions (*, $Eo = 0.4$, $Mo = 1.1 \times 10^{-6}$, $Re_\infty = 17$; ×, $Eo = 0.1$, $Mo = 3.9 \times 10^{-10}$, $Re_\infty = 99$).

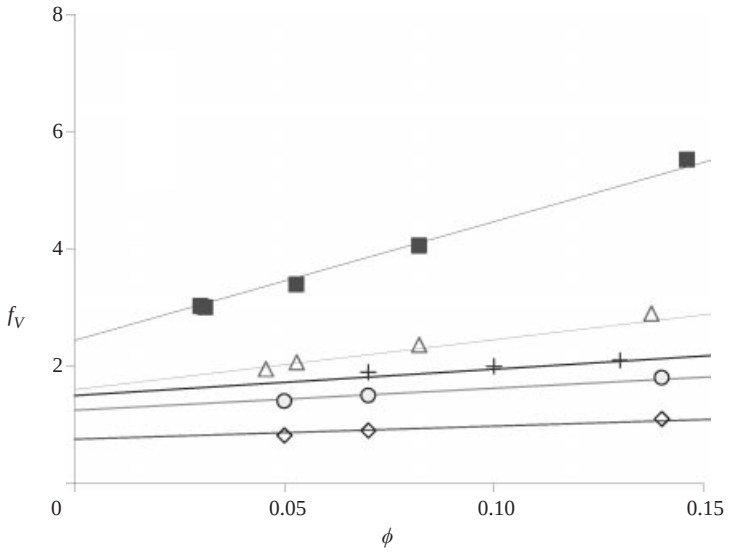

FIGURE 19. Virtual mass coefficients for distorted bubbles vs. bubble volume or area fraction, ϕ. One bubble per box. △, two-dimensional ellipse, $Eo = 6.8$, $Mo = 7.2 \times 10^{-3}$, $Re_\infty = 5$; +, two-dimensional shedding ellipse, $Eo = 11.9$, $Mo = 5 \times 10^{-8}$, $Re_\infty = 170$; ■, two-dimensional circular cap, $Eo = 11.2$, $Mo = 7.2 \times 10^{-3}$, $Re_\infty = 7.2$; ◇, three-dimensional ellipsoid (non shedding), $Eo = 5$, $Mo = 5.1 \times 10^{-6}$, $Re_\infty = 70$; and ○, three-dimensional ellipsoid (non shedding), $Eo = 2$, $Mo = 2 \times 10^{-8}$, $Re_\infty = 176$.

Extrapolation of the results to $\phi = 0$ yields f_{V0} values of 0.5 (spherical) and 1.0 (circular). Lines in this figure represent linear fits of the data, satisfying theoretical f_{V0} values.

Figure 19 shows results obtained with distorted bubbles. The intercept, f_{V0}, clearly depends on Eo and Mo.

Figure 20 shows a plot of f_{V0}/Δ ($\Delta = 1$ for two dimensions, and 0.5 for three

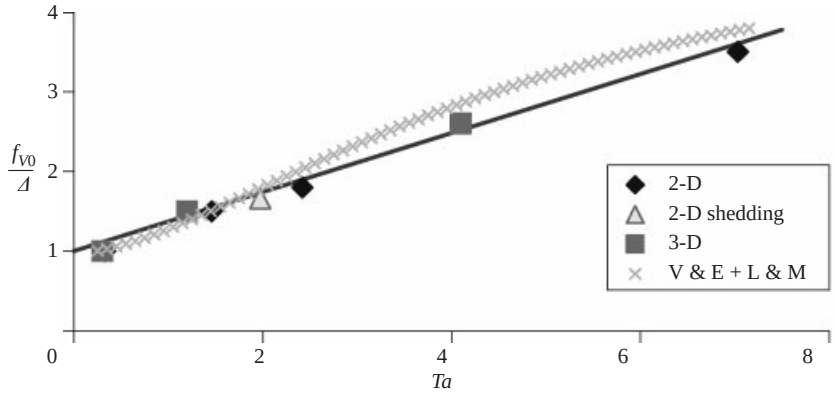

FIGURE 20. Single bubble virtual mass coefficients in two and three dimensions vs. Ta ($=Re\,Mo^{0.23}$), $\times$, virtual mass coefficient for a spheroid (Lai & Mockros 1972) based on aspect ratio given by Vakhrushev & Efremov (1970). Solid line: linear fit.

dimensions) obtained from figure 19, against Ta. The solid line represents a linear fit

$$\frac{f_{V0}}{\Delta} = 0.37Ta + 1. \tag{38}$$

Recall that Ta was used earlier to describe the deformation of the bubble (see figure 11). Equation (38) suggest that f_{V0} increases as the bubble becomes more deformed and that the variation of f_{V0} shown in figure 20 can be correlated with the aspect ratio of isolated bubbles.

Lai & Mockros (1972) deduced the virtual mass coefficient for solid spheroids by analysing their oscillatory motion in Stokes flow. We used the correlation due to Vakhrushev & Efremov (1970) (and modified by Fan & Tsuchiya 1990) to estimate the aspect ratio (see figure 11 presented earlier). We then computed the virtual mass coefficient for a solid spheroid with this aspect ratio, using the expression derived by Lai & Mockros (1972). This result is also shown in figure 20. This analysis reveals that the variation of f_{V0} shown in figures 18 and 19 can be correlated with the aspect ratio of isolated bubbles.

At the same time, aspect ratio does not appear to be an appropriate measure for estimating the virtual mass coefficients in an ordered array of bubbles. For example, it was shown earlier in figure 14 that the aspect ratio of the bubble (for the combination of parameters shown in the caption of that figure) increased dramatically with ϕ. If aspect ratio were an adequate means of correlating virtual mass coefficients, we would have seen a decrease in the virtual mass coefficient with increasing ϕ in that example. As shown in figure 14, this is not the case.

The quantity f_{V0} can be used to normalize the results of the distorted and non-distorted bubbles. These normalized results are given in figure 21. The solid line which seems to describe the results quite well in three dimensions is given by

$$\frac{f_V}{f_{V0}} = 1 + 4\phi. \tag{39}$$

Equations (38) and (39) may be used as computationally generated closures for the virtual mass coefficient in the region $0 < \phi < 0.2$.

A parity plot comparing virtual mass coefficient obtained from (38) and (39) with those estimated from simulations is shown in figure 22.

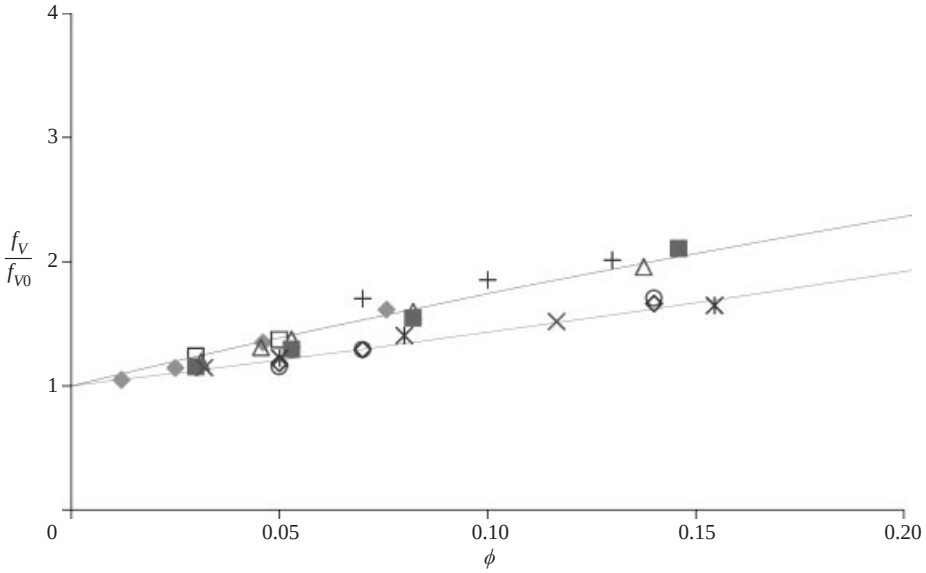

FIGURE 21. Normalized virtual mass coefficients for two- and three-dimensional systems: deformed and non-deformed bubbles in regular arrays. Symbols: see figures 18 and 19.

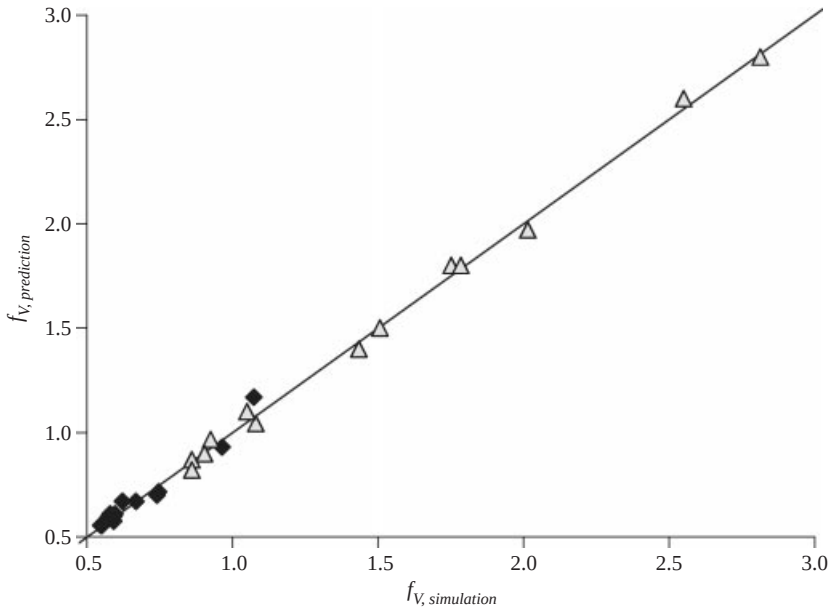

FIGURE 22. Parity plot comparing virtual mass coefficients predicted by (38) and (39) with those estimated from simulations: △, cooperative rise; ◆, hindered rise (see figure 16*b*).

7. Effect of orientation on drag and virtual mass

In all the simulations presented thus far, the bubbles were aligned in the direction of gravity. We performed a limited exploration of the effect of the orientation of the ordered array of bubbles with respect to the gravitational direction on the rise behaviour. This can be achieved by tilting the orientation of gravity in our simulation of a single bubble in a periodic box. This line of investigation was suggested to the

authors by Professor A. S. Sangani. An illustration of this is presented in figure 23(*a*), which shows the streamlines (at one particular instant of time), for the same case as in figure 13, but for a different orientation of gravity. In this case, the bubbles assume an asymmetric shape, with the nose of every bubble being pulled towards the wake of the preceding bubble. Furthermore, the assembly of bubbles migrated obliquely to the direction of gravity. The component of the scaled rise velocity in the $-\boldsymbol{g}$-direction, $v_{\parallel}d_e/\nu = Re_{\parallel}$ and that in the direction perpendicular to gravity, $v_{\perp}d_e/\nu = Re_{\perp}$ are indicated in figure 23(*a*). Their values for various orientations of gravity are shown in figure 23(*b*). The results shown in figure 23(*b*) for $0 \leqslant \alpha < 45^{\circ}$ were reproducible from different initial conditions. Furthermore, the same value of $Re_{\parallel}$ was obtained for orientations α and $90^{\circ} - \alpha$ (for $0 \leqslant \alpha \leqslant 40^{\circ}$), while the perpendicular components of the velocities had opposite signs. At $\alpha = 45^{\circ}$, where one would have expected $Re_{\perp}$ to be zero, a non-zero value of $Re_{\perp}$ whose sign depended on the initial condition was obtained. Clearly, the symmetric flow solution (with $Re_{\perp} = 0$) was unstable, giving way to a pair of oblique solutions (see figure 23*b*). We did not pursue a detailed investigation of this bifurcation behaviour. This procedure was repeated in three-dimensional simulations as well, where we examined whether the cooperative rise behaviour (i.e. $n < 1$) persisted for all orientations of gravity. Figure 24 shows $Re_{\parallel}$ values obtained in three-dimensional simulations at various bubble volume fractions and orientations of gravity. Simulations were performed for 13 different orientations of gravity, denoted in this figure by a pair of angles (α_1, α_2). Here, α_1 is the angle between $-\boldsymbol{g}$ and the z-axis and α_2 denotes the angle between the x-axis and the projection of $-\boldsymbol{g}$ on the (x, y)-plane (with the x, y and z directions being aligned with the edges of the periodic box). As in the two-dimensional example, the rise velocity changed with orientation of gravity. However, it is clear from figure 24 that the cooperative rise behaviour persisted for every orientation of gravity examined. In this figure, for the sake of clarity, we have shown the linear fits for only two cases. Good linear fits were obtained for the other cases as well. The Richardson–Zaki exponent ranged from -4.5 to -3.6 in these simulations, depending on the orientation of gravity. The two lines shown in this figure correspond to these two extrema.

When the bubbles are distorted, the virtual mass coefficient manifested a small dependence on the orientation of gravity relative to the directions associated with the periodic box. This is illustrated in figure 25 for a two-dimensional simulation.

8. Multi-bubble simulations

All the simulations discussed thus far focused on the flow behaviour of a single bubble in a periodic box, and therefore the results extracted from such simulations are restricted to a regular array of bubbles. Esmaeeli & Tryggvason (1996, 1998, 1999) examined the motion of a swarm of freely evolving bubbles in a periodic domain using direct numerical simulation of the Navier–Stokes equations using the finite difference/front tracking method. They found that the effective rise velocity of a freely evolving swarm was, in general, different from that of a regular array.

A freely evolving swarm of nearly circular two-dimensional bubbles rising in a liquid at $Re \approx 2$ (corresponding to $Mo = 10^{-3}$ and $Eo = 1$) rose faster than a regular array of bubbles at the same bubble fraction, while this difference appeared to be smaller in three-dimensional simulations (Esmaeeli & Tryggvason 1998). A regular array of bubbles, when allowed to evolve freely, was unstable and bubble–bubble interaction occurred by kissing, drafting and tumbling (Fortes, Joseph & Lundgren 1987). Esmaeeli & Tryggvason also found that the rise velocity in their

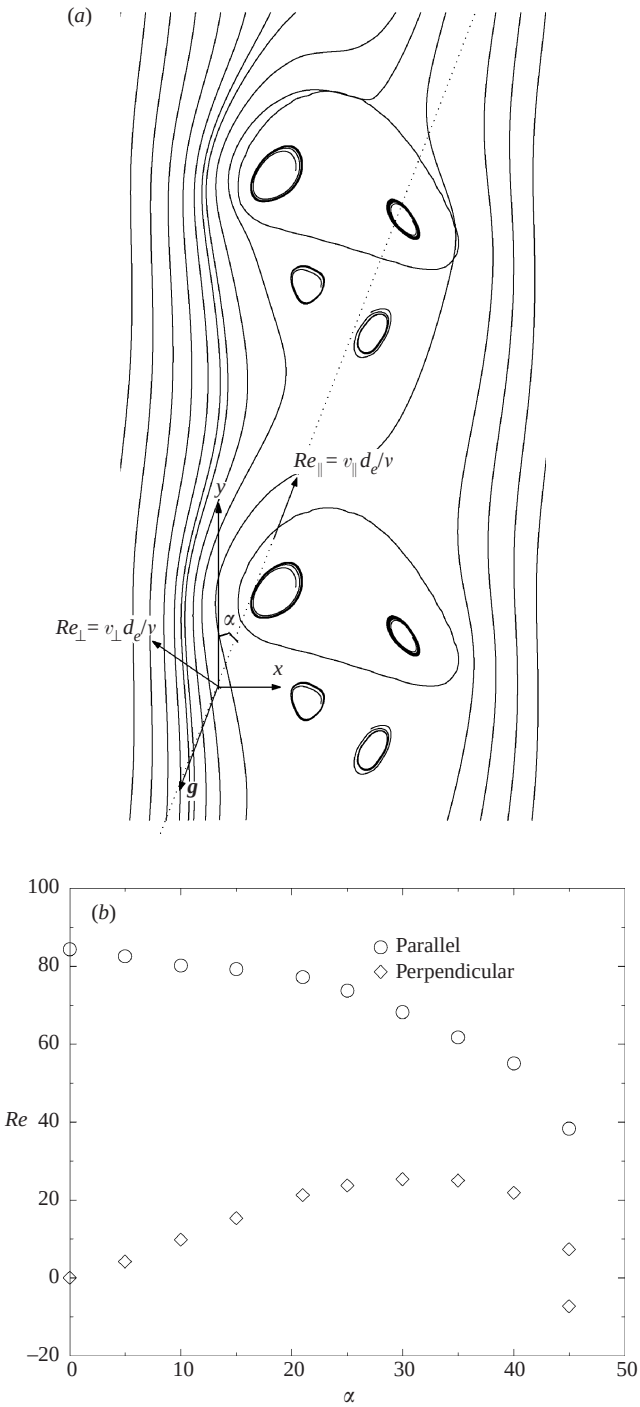

FIGURE 23. (*a*) 'Streamlines' for bubble rise at bubble area fraction of 0.15 showing asymmetric wake structures. 50×50 nodes. Two periodic boxes. Gravity pointing at an angle of 21° to the vertical as shown by the arrow. $Mo = 10^{-5}$, $Eo = 1.2$. (*b*) $Re_{\parallel}$ and $Re_{\perp}$ for various orientations (α_1, α_2) of gravity. Bubble area fraction 0.15, $Mo = 10^{-5}$, $Eo = 1.2$. 50×50 nodes.

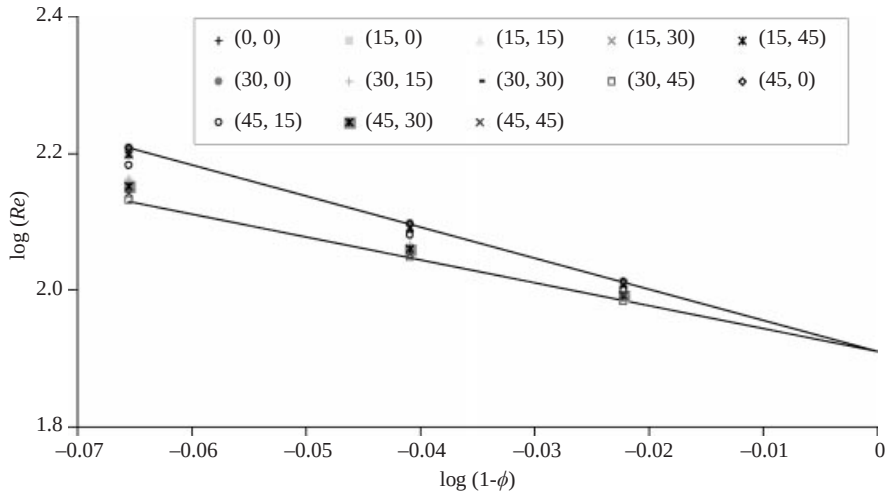

FIGURE 24. Dimensionless rise velocity, $Re_{\|}$, for various orientations and volume fractions. Single bubble in a periodic box. $Mo = 7.2 \times 10^{-4}$, $Eo = 53$. x, y, z directions are aligned with the edges of the periodic box. α_1 is angle between $-\boldsymbol{g}$-direction and z-axis. α_2 is angle between x-axis and the projection of $-\boldsymbol{g}$ on to the (x, y)-plane. The minimal and maximal slope are -4.5 and -3.6.

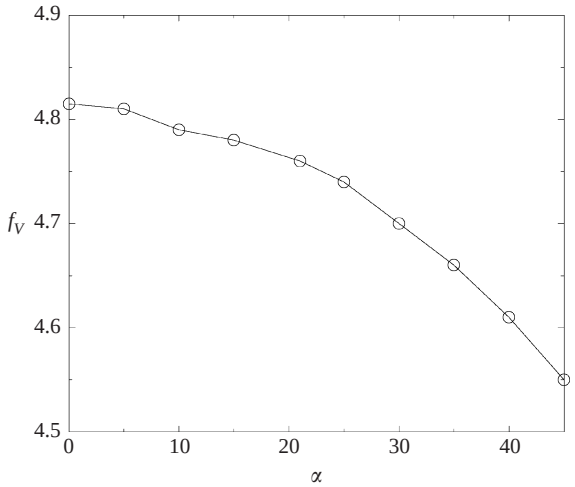

FIGURE 25. Virtual mass coefficient for a two-dimensional system (described in figure 23*a*,*b*) as a function of angle α. Solid lines are drawn to guide the eye.

two-dimensional simulations increased steadily with system size (without appearing to level off) and this was accompanied by an increase in the kinetic energy associated with the fluctuating motion of the liquid phase. They observed flow structures that extended over several bubble diameters and the energy spectrum revealed a $-5/3$ slope over a range of wavenumbers, reminiscent of forced two-dimensional turbulence.

Esmaeeli & Tryggvason (1999) simulated the rise behaviour of distorted bubbles at $Re \approx 20$–30 (corresponding to $Mo = 10^{-5}$ and $Eo = 2$) and found that a freely evolving swarm tended to rise more slowly than a regular array, which is opposite of the effect seen with nearly circular (spherical) bubbles. In one set of simulations exploring

the effect of system size on the flow behaviour of freely evolving swarm of two-dimensional bubbles, the rise velocity was found to be roughly independent of system size when there were four or more freely evolving bubbles in the periodic box. However, the kinetic energy of the liquid phase increased monotonically with system size.

In all the simulations of Esmaeeli & Tryggvason (1996, 1998, 1999), the rise velocity of a regular or freely evolving swarm of bubbles always decreased when the bubble fraction was increased. The cooperative rise behaviour observed in our simulations occurred at larger values of χ ($= Re\, Mo^{1/4} Eo^{-1/2}$) than encountered in their study.

In any case, the results of Esmaeeli & Tryggvason (1996, 1998, 1999) clearly reveal that the closure relations obtained in the present manuscript for regular swarms of bubbles are not reliable for freely evolving bubble swarms. We performed a limited number of multi-bubble simulations in an attempt to repeat some of the calculations reported by Esmaeeli & Tryggvason (1996, 1998, 1999). An illustration in two dimensions with 16 freely evolving bubbles is presented in figures 26 and 27. In these simulations, a 200×200 periodic box was initially partitioned into sixteen 50×50 square arrays and a bubble was placed randomly inside each of these squares. The sixteen bubbles were then allowed to rise under the action of buoyancy and evolve freely in the 200×200 periodic box. Figure 26 shows the average rise velocity of the swarm of bubbles (expressed as a Reynolds number) in five different realizations. Also shown in this figure is the result obtained in a regular array (i.e. a single bubble in a periodic box at an equivalent bubble fraction). Note that in all the cases, the Reynolds number increases rapidly at first and reached the same plateau. At a somewhat later time, the rise velocity of the freely evolving swarm drifts away from this plateau and begins to fluctuate with a substantial amplitude.

The Reynolds number estimated from the five runs is shown in this figure as broken line and it represents a (limited) ensemble-average. The ensemble-average Re shows smaller temporal fluctuations than the individual realizations (in the time window shown). In any case, the average rise velocity of this freely evolving swarm (obtained by averaging the ensemble-average rise velocity from $tv/d_e^2 = 15$ to $tv/d_e^2 = 30$) is larger than the rise velocity of a regular array of bubbles, which is consistent with the observation of Esmaeeli & Tryggvason (1998) for nearly circular bubbles. For the same combination of Eo, Mo, bubble fraction and number of freely evolving bubbles in the box, Esmaeeli & Tryggvason (1998) obtained an average Re of 1.63, while our simulations yielded a value of 1.64. For a regular array, Esmaeeli & Tryggvason (1998) found Re to be 1.35, while our LBM simulations gave a value of 1.39. These are very close, providing additional confidence in our results. (We mention in passing that we have employed d_e^2/v as characteristic time, while Esmaeeli & Tryggvason used $(d_e/g)^{0.5}$ to make time dimensionless. Our simulations shown in figure 26 were run for essentially the same length of time as that of Esmaeeli & Tryggvason.) In the simulations shown in figure 26, the bubbles travelled a distance of 4 box heights in approximately 30 units of dimensionless time.

The rise behaviour manifested in one of these five simulations is reproduced in figure 27, where we also show the configurations at four different instants of time. It is clear that the simulation did sample a number of close encounters between the bubbles. However, it must be remarked that freely evolving multi-bubble simulations sooner or later led to bubble coalescence in our LBM calculations. This proved to be a severe limitation and we were able to obtain multi-bubble simulation results only for a handful of cases involving nearly circular (two-dimensional) or nearly spherical (three-dimensional) bubbles. Although simulations could be repeated readily for a large number of initial configurations, each simulation generally sampled only a very

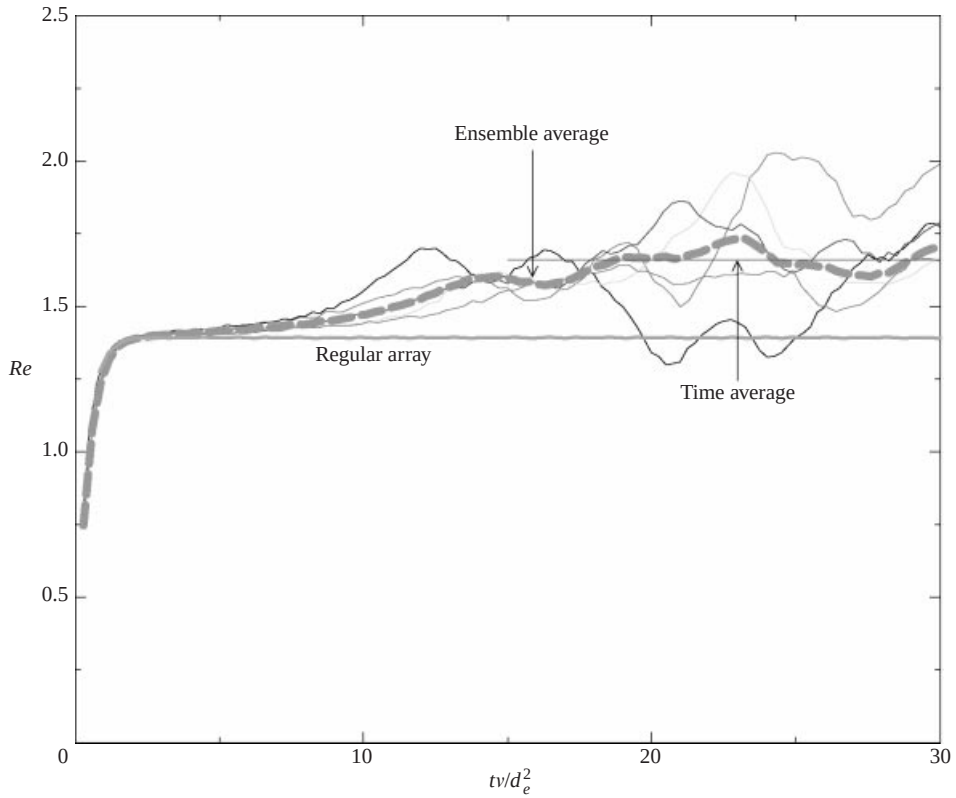

FIGURE 26. Temporal evolution of the average rise velocity of a freely evolving swarm of bubbles. Two-dimensional simulation involving 16 bubbles were performed using 200×200 grids. This domain was divided into sixteen 50×50 grids and a circular bubble was placed randomly in each of them. Then gravity was turned on and the system was allowed to evolve freely in the 200×200 periodic box. $Mo = 10^{-3}$, $Eo = 1$. The solid lines showing appreciable temporal fluctuations at later times represent five different realizations, corresponding to five different initial conditions. The broken grey line (marked ensemble average) represents an average of these five runs. Time average denotes the mean value obtained by averaging the ensemble average between 15 and 30 dimensionless time units. The figure also shows the behaviour of a regular array, obtained by simulating a single bubble in a 50×50 periodic box.

limited number of bubble–bubble interactions before coalescence occurred. Therefore, the average rise velocity obtained from such simulations may not represent a good estimate of the true rise velocity of a freely evolving swarm of bubbles. The latter can be obtained only when a large number of bubble–bubble interactions are sampled in a given simulation. The example shown in figures 26 and 27 is one of a few cases where we were able to continue the simulations for a fairly long duration. Even in this example, we had to run simulations for several tens of initial conditions before we could obtain five runs, in which no coalescence occurred during the first 30 units of dimensionless time.

Coalescence was invariably very rapid in our LBM simulations involving distorted bubbles and at least one coalescence event occurred by the time the bubbles had travelled one box height. Therefore, we were unable to generate any results for a freely evolving swarm of such bubbles. The cooperative rise behaviour observed in our simulations of ordered arrays of highly distorted bubbles is rather intriguing and

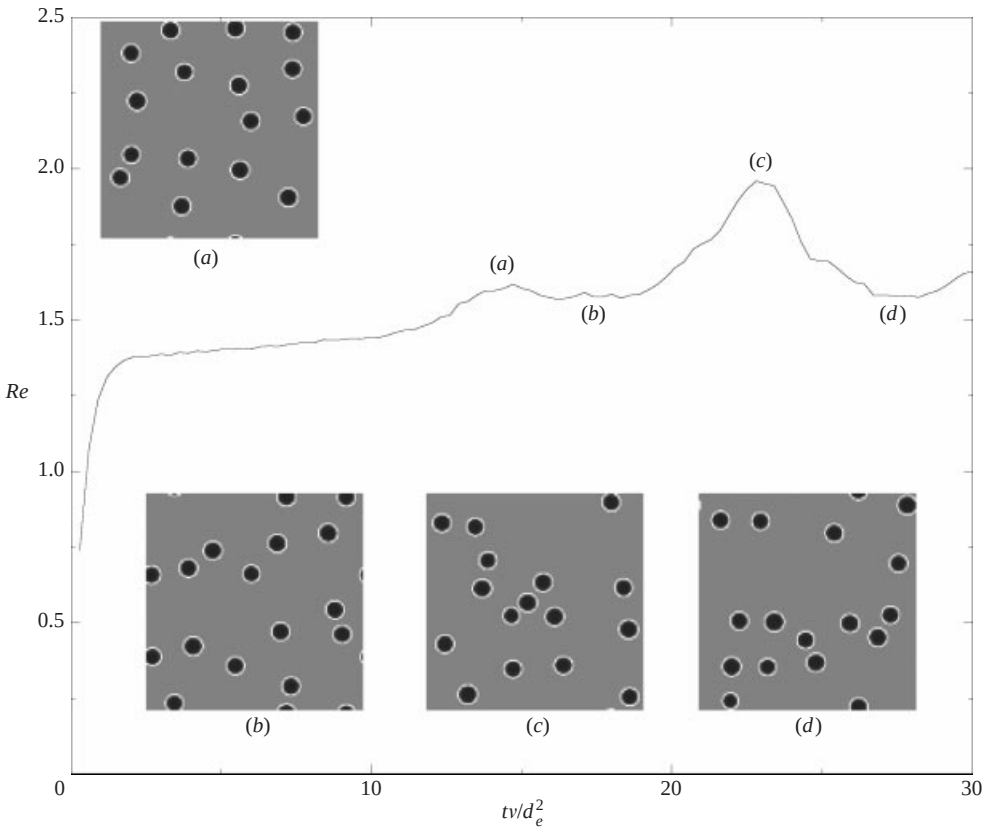

FIGURE 27. As figure 26 but for only one of the five realizations shown. The four insets show the configurations of bubbles at four different dimensionless times: (*a*) 14, (*b*) 17, (*c*) 22, (*d*) 27.

it will be interesting to see if this behaviour persists even in the case of a freely evolving swarm of such bubbles.

9. Summary

The main results of this paper on closure for drag force and on virtual mass coefficient are summarized in (34)–(39). These relations are limited to a regular array of uniformly sized bubbles dispersed in a liquid. To the best of our knowledge, this is the first time a comprehensive model for drag force that spans the entire range from hindered to cooperative motion of bubble swarms is presented in the literature.

The aspect ratio of bubbles is a useful measure to correlate the virtual mass coefficient of isolated bubbles, but not bubble swarms.

The closures were derived via computational experiments based on the lattice Boltzmann method using a BGK collision model. We found the conventional explicit LBM scheme to be suitable for simulating efficiently bubble motion only over a relatively narrow range of Eo and Mo values. The implicit lattice Boltzmann scheme dramatically expanded the range of Eo and Mo values which could be investigated economically.

Simulation of a freely evolving swarm of equally sized bubbles proved to be difficult because of the tendency of the bubbles to coalesce. Consequently, we could

not investigate in a conclusive manner how the closure relations presented here should be modified for freely evolving swarms. It will be particularly interesting to see if the regime of cooperative rise exists for a freely rising swarm of identical bubbles.

We are grateful to the NEC Research Institute, Princeton NJ, for allowing us to use their computational facilities.

REFERENCES

van den Akker, H. E. A. 1998 Coherent structures in multiphase flows. *Powder Tech.* **100**, 123–136.

Auton, T. R., Hunt, J. C. R. & Prud'homme, M. 1988 The force exerted on a body in inviscid unsteady nonuniform rotational flow. *J. Fluid Mech.* **197**, 241–257.

Basset, A. B. 1888 *A Treatise on Hydrodynamics*, vol. 2. Dover.

van Baten, J. M. & Krishna, R. 2000 Modelling sieve tray hydraulics using computational fluid dynamics. *Chem. Engng J.* **77**, 143–152.

Bhatnagar, P. L., Gross, E. P. & Krook, M. 1954 A model for collision processes in gases. I. Small amplitude processes in charged and neutral one-component system. *Phys. Rev.* **94**, 511–525.

Biesheuvel, A. & Spoelstra, S. 1989 The added mass coefficient of a dispersion of spherical gas bubbles in liquid. *Intl J. Multiphase Flow* **15**, 911–924.

Bulthuis, H. F., Prosperetti, A. & Sangani, A. S. 1995 Particle stress in disperse two-phase potential flow. *J. Fluid Mech.* **294**, 1–16.

Chen, S. & Doolen, G. 1998 Lattice Boltzmann method for fluid flows. *Annu. Rev. Fluid. Mech.* **30**, 329–364.

Clift, R., Grace, J. R. & Weber, M. E. 1978 *Bubbles, Drops, and Particles.* Academic.

Drew, D. A. 1971 Averaged field equations for two phase media. *Stud. Appl. Maths* **50**, 133–166.

Drew, D. A. & Segel, L. A. 1971 Averaged equations for two phase flows. *Stud. Appl. Maths* **50**, 205–231

Esmaeeli, A. & Tryggvason, G. 1996 An inverse energy cascade in two-dimensional, low Reynolds number bubbly flows. *J. Fluid Mech.* **314**, 315–330.

Esmaeeli, A. & Tryggvason, G. 1998 Direct numerical simulation of bubbly flows. Part 1. Low Reynolds number arrays. *J. Fluid Mech.* **377**, 313–345.

Esmaeeli, A. & Tryggvason, G. 1999 Direct numerical simulation of bubbly flows. Part 2. Moderate Reynolds number arrays. *J. Fluid Mech.* **385**, 325–358.

Fan, L.-S. & Tsuchiya, K. 1990 *Bubble Wake Dynamics in Liquids and Liquid–Solid Suspensions.* Butterworth-Heinemann.

Felderhof, B. U. 1991 Virtual mass and drag in two-phase flow. *J. Fluid Mech.* **225**, 177–196.

Fortes, A., Joseph, D. D. & Lundgren, T. 1987 Nonlinear mechanics of fluidization of beds of spherical particles. *J. Fluid Mech.* **77**, 467–483.

Gustensen, A. K., Rothman, D. H., Zaleski, S. & Zanetti, G. 1991 Lattice Boltzmann model of immiscible fluids. *Phys. Rev.* A **43**, 4320–4327.

Harper, J. F. & Moore, D. W. 1968 The motion of a spherical liquid drop at high Reynolds number. *J. Fluid Mech.* **32**, 367–391.

He, X. & Luo, L.-S. 1997*a* Theory of the lattice Boltzmann method: From the Boltzmann equation to the lattice Boltzmann equation. *Phys. Rev.* E **56**, 6811–6817.

He, H. & Luo, L.-S. 1997*b* A priori derivation of the lattice Boltzmann equation. *Phys. Rev.* E **55**, R6333–R6336.

He, X., Shan, X. & Doolen, G. 1998 Discrete Boltzmann equation model for non-ideal gases. *Phys. Rev.* E **57**, R13–R16.

Hill, M. J. M. 1894 On a spherical vortex. *Phil. Trans. R. Soc. Lond.* **185**, 213–245.

Huang, K. 1987 *Statistical Mechanics.* John Wiley & Sons.

Huo, S., Shan, X., Zou, Q., Doolen, G. D. & Soll, W. E. 1997 Evaluation of two lattice Boltzmann models for multiphase flows. *J. Comput. Phys.* **138**, 695–713.

Jakobsen, H. A., Sannaes, B. H., Grevskott, S. & Svendsen H. F. 1997 Modeling of vertical bubble-driven flows. *Indust. Engng Chem. Res.* **36**, 4052–4072.

Kang, S. Y., Sangani, A. S., Tsao, H. K. & Koch, D. L. 1997 Rheology of dense suspensions. *Phys. Fluids* **9**, 1540–1561.

KATO, Y., KONO, K., SETA, T., MARTINEZ, D. & CHEN, S. 1997 Amadeus project and microscopic simulation of two-phase flow by the lattice-Boltzmann method. *Intl J. Mod. Phys.* C **8**, 843–858.

KRISHNA, R., URSEANU, M. I., VAN BATEN, J. M. & ELLENBERGER, J. 1999 Rise velocity of a swarm of large gas bubbles in liquids. *Chem. Engng Sci.* **54**, 171–183.

LAI, R. Y. S. & MOCKROS, L. F. 1972 The Stokes-flow drag on prolate and oblate spheroids during axial translatory accelerations. *J. Fluid Mech.* **52**, 1–15.

LALLEMAND, P. & LUO, L.-S. 2000 Theory of the lattice Boltzmann method: Dispersion, dissipation, isotropy, Galilean invariance, and stability. *Phys. Rev.* E **61**, 6546–6562.

LAMB, H. 1932 *Hydrodynamics*, 6th Edn, pp. 77 & 124. Dover (reprinted 1997).

LEAL, G. L. 1992 *Laminar Flow and Convective Transport Processes.* Butterworth-Heinemann.

MARTYS, N. S., SHAN, X. & CHEN, H. 1998 Evaluation of the external force term in the discrete Boltzmann equation. *Phys. Rev.* E **58**, 6855–6857.

MOORE, D. W. 1959 Rise of a gas bubble in a viscous liquid. *J. Fluid Mech.* **6**, 113–130.

MOORE, D. W. 1963 The boundary layer on a spherical gas bubble. *J. Fluid Mech.* **16**, 161–176.

NIGMATULIN, R. I. 1979 Spatial averaging in the mechanics of heterogeneous and dispersed systems. *Intl J. Multiphase Flow* **5**, 353–385.

NOURGALIEV, R. R., DINH, T. N. & SEHGAL, B. R. 2001 On lattice Boltzmann modeling of phase transition in an isothermal non-ideal fluid. *J. Comput. Phys.* (submitted).

PARLANGE, J.-Y. 1970 Spherical cap bubbles with laminar wakes. *J. Fluid Mech.* **37**, 257–263.

RICHARDSON, J. F. & ZAKI, W. N. 1954 Sedimentation and fluidization. *Trans. Inst. Chem. Engrs* **32**, 35–53.

ROWLINSON, J. S. & WIDOM, B. 1982 *Molecular Theory of Capillarity, International Series of Monographs on Chemistry.* Clarendon.

SANGANI, A. S. & DIDWANIA, A. K. 1993*a* Disperse phase stress tensor in flows of bubbly liquids at large Reynolds number. *J. Fluid Mech.* **248**, 27–54.

SANGANI, A. S. & DIDWANIA, A. K. 1993*b* Dynamic simulations of flows of bubbly liquids at large Reynolds number. *J. Fluid Mech.* **250**, 307–337.

SANGANI, A. S., ZHANG, D. Z. & PROSPERETTI, A. 1991 The added mass, Basset, and viscous drag coefficients in nondilute bubbly liquids undergoing small-amplitude oscillatory motion. *Phys. Fluids* A **3**, 2955–2970.

SANKARANARAYANAN, K., SHAN, X., KEVREKIDIS, I. G. & SUNDARESAN, S. 1999 Bubble flow simulations with the Lattice Boltzmann method. *Chem. Engng Sci.* **54**, 4817–4823.

SHAN, X. & CHEN, H. 1993 Lattice Boltzmann model for simulating flows with multiple phases and components. *Phys. Rev.* E **47**, 1815–1819.

SHAN, X. & DOOLEN, G. 1995 Multicomponent Lattice Boltzmann model with interparticle interaction. *J. Statist. Phys.* **81**, 379–393.

SHAN, X. & HE, X. 1998 Discretization of the velocity space in the solution of the Boltzmann equation. *Phys. Rev. Lett.* **8**, 65–68.

SPELT, P. D. M. & SANGANI, A. S. 1998 Properties and averaged equations for flows of bubbly liquids. *Appl. Sci. Res.* **58**, 337–386.

STERLING, J. D. & CHEN, S. 1996 Stability analysis of lattice Boltzmann methods. *J. Comput. Phys.* **123**, 196–206.

STROUD, A. H. 1971 *Approximate Calculation of Multiple Integrals.* Prentice-Hall.

SWIFT, M. R., ORLANDINI, S. E., OSBORN, W. R. & YEOMANS, J. M. 1996 Lattice Boltzmann simulations of liquid–gas and binary-fluid systems. *Phys. Rev.* E **54**, 5041–5052.

SWIFT, M. R., OSBORN, W. R. & YEOMANS, J. M. 1995 Lattice Boltzmann simulation of non-ideal fluids. *Phys. Rev. Lett.* **75**, 830–833.

VAKHRUSHEV, I. A. & EFREMOV, G. I. 1970 *Chem. Technol. Fuels Oils* (*USSR*) **5/6**, 376–379. Cited by Fan & Tsuchiya (1990).

VAN WIJNGAARDEN, L. 1976 Hydrodynamic interaction between gas bubbles in liquid. *J. Fluid Mech.* **77**, 27–44.

WILKINSON, P. M., SPEK, A. P. & VAN DIERENDONCK, L. L. 1992 Design parameters estimation for scale-up of high-pressure bubble columns. *AIChE J.* **38**, 544–554.

WORTHING, R. A., MOZER, J. & SEELEY, G. 1997 Stability of lattice Boltzmann methods in hydrodynamic regimes. *Phys. Rev.* E **56**, 2243–2253.

Yuan H. & Prosperetti, A. 1994 On the in-line motion of two spherical bubbles in a viscous fluid. *J. Fluid Mech.* **278**, 325–349.

Zhang, D. Z. & Prosperetti, A. 1994 Ensemble phase averaged equations for bubbly flows. *Phys. Fluids* **6**, 2956–2970.

Zhang, D. Z. & Prosperetti, A. 1997 Momentum and Energy equations for disperse two-phase flows and their closures for dilute dispersions. *Intl J. Multiphase Flow* **23**, 425–453.

Zuber, N. 1964 On the dispersed two-phase flow in the laminar flow regime. *Chem. Engng Sci.* **19**, 897–917.